

Article

Crystal Structure of Bismuth-Containing Samarium Iron–Aluminium Borates $\text{Sm}_{1-x}\text{Bi}_x\text{Fe}_{3-y}\text{Al}_y(\text{BO}_3)_4$ ($x = 0.05\text{--}0.07$, $y = 0\text{--}0.28$) in the Temperature Range of 25–500 K

Ekaterina S. Smirnova ^{1,*}, Olga A. Alekseeva ¹, Vladimir V. Artemov ¹, Timofei A. Sorokin ¹, Dmitry N. Khmelenin ¹, Ekaterina V. Sidorova ¹, Kirill V. Frolov ¹ and Irina A. Gudim ²

¹ Shubnikov Institute of Crystallography of Federal Scientific Research Centre ‘Crystallography and Photonics’, Russian Academy of Sciences, Moscow 119333, Russia; olalex@crys.ras.ru (O.A.A.)

² Kirensky Institute of Physics, Federal Research Center KSC SB RAS, Krasnoyarsk 660036, Russia; bezm@iph.krasn.ru

* Correspondence: esmi@ns.crys.ras.ru

Abstract: Structural features of new mixed bismuth-containing samarium iron–aluminium borate single crystals $\text{Sm}_{1-x}\text{Bi}_x\text{Fe}_{3-y}\text{Al}_y(\text{BO}_3)_4$ ($x = 0.05\text{--}0.07$, $y = 0\text{--}0.28$) were studied using X-ray diffraction analysis based on aluminium content and temperature in the range 25–500 K. The crystals were grown using the solution-in-melt technique with $\text{Bi}_2\text{Mo}_3\text{O}_{12}$ in a flux. The composition of the single crystals was analyzed using energy-dispersive X-ray fluorescence and energy-dispersive X-ray elemental analysis. Temperature dependencies of $\text{Sm}_{1-x}\text{Bi}_x\text{Fe}_{3-y}\text{Al}_y(\text{BO}_3)_4$ unit-cell parameters were studied. Negative thermal expansion was identified below 100 K and represented by characteristic surfaces of the thermal expansion tensor. (Sm,Bi)–O, (Sm,Bi)–(Fe,Al), (Fe,Al)–(Fe,Al), and (Fe,Al)–O interatomic distances decreased with the addition of aluminium atoms. An increase in the (Fe,Al)–(Fe,Al) intrachain bond length at low temperatures in the magnetically ordered state weakened this bond, whereas a decrease in the (Fe,Al)–(Fe,Al) interchain distance strengthened super-exchange paths between different chains. It was found that the addition of aluminium atoms influenced interatomic distances in $\text{Sm}_{1-x}\text{Bi}_x\text{Fe}_{3-y}\text{Al}_y(\text{BO}_3)_4$ much more than lowering the temperature from 293 K to 25 K. The effect of aluminium doping on magnetoelectric properties and structural symmetry of rare-earth iron borates is also discussed.

Keywords: rare-earth iron–aluminium borates; solid solutions; low-temperature X-ray diffraction; single crystals; temperature structural dynamics; negative thermal expansion



Citation: Smirnova, E.S.; Alekseeva, O.A.; Artemov, V.V.; Sorokin, T.A.; Khmelenin, D.N.; Sidorova, E.V.; Frolov, K.V.; Gudim, I.A. Crystal Structure of Bismuth-Containing Samarium Iron–Aluminium Borates $\text{Sm}_{1-x}\text{Bi}_x\text{Fe}_{3-y}\text{Al}_y(\text{BO}_3)_4$ ($x = 0.05\text{--}0.07$, $y = 0\text{--}0.28$) in the Temperature Range of 25–500 K. *Crystals* **2023**, *13*, 1128. <https://doi.org/10.3390/cryst13071128>

Academic Editor: László Kovács

Received: 21 June 2023

Revised: 12 July 2023

Accepted: 15 July 2023

Published: 19 July 2023



Copyright: © 2023 by the authors. Licensee MDPI, Basel, Switzerland. This article is an open access article distributed under the terms and conditions of the Creative Commons Attribution (CC BY) license (<https://creativecommons.org/licenses/by/4.0/>).

1. Introduction

Complex borates with a general formula of $\text{RM}_3(\text{BO}_3)_4$ ($R = \text{La}\text{--}\text{Lu}$, Y ; $M = \text{Al}$, Fe , Cr , Ga , Sc) and their solid solutions are promising materials for lasers, nonlinear optics, spintronics, and photonics since they are characterized by multifunctional properties depending on their composition and crystal structures [1].

Crystals from the rare-earth iron borate family $\text{RFe}_3(\text{BO}_3)_4$ with subsystems of different magnetic ions (R and Fe) are attributed to the multiferroics due to a wide range of magnetoelectric properties caused by the complex exchange interactions between the magnetic subsystems that are responsible for the magnetic structure (easy-plane, easy-axis, or more complex arrangements of magnetic ions), the magnitude of magnetoelectric and magnetoelastic effects, the presence and temperature of spin-reorientation transition, structure phase transition, and magnetic phase transition [2–9].

Rare-earth aluminium borates $\text{RAI}_3(\text{BO}_3)_4$ with only magnetic subsystem (R) combine luminescent and pronounced nonlinear optical properties and exhibit giant magnetoelectric effects with induced polarization values that are higher than for iron borates [10,11].

YAl₃(BO₃)₄ with different doping activators is a non-linear material that is widely used in lasing technology [12].

The type of rare-earth atoms in RM₃(BO₃)₄ influences their crystal structure. Currently, RM₃(BO₃)₄ crystals are synthesized in trigonal crystal systems (*R*32, *P*3₁21, *P*321 space groups) or monoclinic crystal systems (*C*2/*c*, *C**c*, and *C*2 space groups) [1].

Rare-earth iron borates RFe₃(BO₃)₄ at high temperatures belong to the trigonal space group *R*32, which persists down to 2–3 K for *R* = La–Sm. There is a structural phase transition from space group *R*32 (at higher temperatures) to space group *P*3₁21 (at lower temperatures) for RFe₃(BO₃)₄ with a smaller ionic radius of rare-earth atom (*R* = Eu–Er), which manifests itself through anomalies in dielectric properties, thermal expansion, and magnetoelectric properties [13]. The temperature of the structural phase transition increases with the decrease in the rare-earth ion radius. The structural features of the phase transition were first described in [14], while distortions in the crystal structure appearing in RFe₃(BO₃)₄ in the *P*3₁21 space group at lower temperatures were discussed later [15]. The iron subsystem in RFe₃(BO₃)₄ becomes antiferromagnetically ordered below *T*_N = 30–40 K, and *f*–*d* exchange interaction between *R* and Fe magnetic moments leads to the different types of magnetic anisotropy and magnetic moment orientation [16]. Various types of spin reorientations appear with a further decrease in temperature [17–20].

Most rare-earth aluminium borates, RAl₃(BO₃)₄, also have a structure type of mineral huntite CaMg₃(CO₃)₄ described by space group *R*32. However, monoclinic modifications (space group *C*2/*c* or *C*2) were discovered for RAl₃(BO₃)₄ (*R* = Pr, Nd, Sm, Eu, Gd, Tb, Ho) crystals and the polytype nature of phases *R*32, *C*2/*c*, and *C*2 was demonstrated [21–23], similar to that in rare-earth chromium borates [24]. Trigonal huntite phase *R*32 may be present in a monoclinic view in accordance with the known transformation of rhombohedral *R*-cell to monoclinic *C*-cell [23].

The quality, structure, and composition of RM₃(BO₃)₄ (*M* = Fe, Al) single crystals are highly dependent on growth techniques [1,25–27]. Rare-earth iron borates RFe₃(BO₃)₄ of the highest quality and with sizes optimal for comprehensive analysis of physical properties were grown using the solution-in-melt technique following the method described in [28–31]. However, using Bi₂Mo₃O₁₂ in a flux led to partial substitution of rare-earth atoms in the structures with ≈4–9% of bismuth atoms [15]. Incorporation of Bi in the RFe₃(BO₃)₄ structure lowered the *R*32→*P*3₁21 transition temperature; however, other structural features associated with bismuth addition have not been identified [29,32]. RAl₃(BO₃)₄ single crystals were grown using the solution-in-melt technique, with different fluxes or annealing of precursors [21–23,33,34]. The formation of monoclinic or trigonal phases was dependent on growth conditions, specifically on the crystallization temperature [22].

SmFe₃(BO₃)₄ single crystals are known to exhibit very large magnetodielectric effects [35]. Magnetoelectric properties of SmFe₃(BO₃)₄ single crystals were found to be dependent on twin components in the crystal structure [29].

The physical properties of SmAl₃(BO₃)₄ have not been studied extensively. Spectroscopic properties of the monoclinic phase of SmAl₃(BO₃)₄ were analyzed in [21] and IR-spectra were measured for trigonal SmAl₃(BO₃)₄ in [22].

Substitution of iron atoms by aluminium atoms in the structure of RFe_{3–*x*}Al_{*x*}(BO₃)₄ can influence the magnetic structure and properties of these crystals. The modification of crystals by diamagnetic ion influences the magnetocrystalline anisotropy, and as a result, transforms the electromagnetic characteristics [36,37]. Diamagnetic substitution in Fe_{1–*x*}Ga_{*x*}BO₃ single crystals influenced Néel temperature and magnetic susceptibility [37]. Ferroelectric properties improved with increased Ti⁴⁺ substitution in Nd³⁺-modified Bi_{0.9}Nd_{0.1}Fe_{1–*x*}Ti_{*x*}O₃ (0.025 ≤ *x* ≤ 0.100) solid solutions [38]. Thin areas of Al–O–Al structures around the magnetic domains in Ni_{0.4}Zn_{0.35}Co_{0.25}Fe_{2–*x*}Al_{*x*}O₄ (0 ≤ *x* ≤ 0.12) ferrite ceramic create obstacles for the movement of domain walls, increasing the coercivities [39].

A comprehensive study of a series of rare-earth iron–aluminium borate RFe_{3–*x*}Al_{*x*}(BO₃)₄ solid solutions is interesting due to possible variation or enhancement of multiferroic and

optical properties induced by competition for Fe and Al ion interactions with neighbouring atoms.

In the present work, we studied the composition and crystal structure of mixed bismuth-containing $\text{Sm}_{1-x}\text{Bi}_x\text{Fe}_{3-y}\text{Al}_y(\text{BO}_3)_4$ single crystals grown for the first time using the solution-in-melt technique, analysed their structural features based on the Al content ($y = 0\text{--}0.28$) and the temperature (25–500 K). Information on the structural evolution of $\text{Sm}_{1-x}\text{Bi}_x\text{Fe}_{3-y}\text{Al}_y(\text{BO}_3)_4$ will be valuable for further studies of multiferroic and optical properties of mixed orthoborates $R_{1-x}R'_xM_{3-y}M'_y(\text{BO}_3)_4$ with different rare-earth and metal elements, including first-principle approaches.

2. Materials and Methods

2.1. Crystal Growth

$\text{SmFe}_{3-y}\text{Al}_y(\text{BO}_3)_4$ ($0 \leq y \leq 0.2$) single crystals were grown from fluxes based on $\text{Bi}_2\text{Mo}_3\text{O}_{12}$ [28,29]. The flux composition in the quasibinary form was $(100 - n)\%_{\text{mass}}\{\text{Bi}_2\text{Mo}_3\text{O}_{12} + p\text{B}_2\text{O}_3 + r\text{Sm}_2\text{O}_3\} + n\%_{\text{mass}} \text{SmFe}_{3-y}\text{Al}_y(\text{BO}_3)_4$, where n is the crystal-forming oxide concentration corresponding to the $\text{SmFe}_{3-y}\text{Al}_y(\text{BO}_3)_4$ stoichiometry and p , q , and r are coefficients. The contents of the flux components and the main crystallization parameters are given in Table 1.

Table 1. Contents of flux components and the crystallization parameters.

y	n	p	r	T_{sat} , °C	dT_{sat}/dn , °C/Mass.%	ΔT_{met} , °C
0	20	2	0.6	977	~5	
0.05	19.8	2	0.6	955	~5.5	
0.1	20.1	2	0.6	960	~5	≈12
0.15	20.2	2	0.6	956	~6	
0.2	23	2.1	0	959	~8	

Areas of $\text{SmFe}_{3-y}\text{Al}_y(\text{BO}_3)_4$ crystal stability and ratios of flux components were defined using the direct phase probing method. The saturation temperature T_{sat} was determined to an accuracy of ± 2 °C using probe crystals that were obtained preliminarily from the same flux under conditions of spontaneous crystallization on a rotating Pt ring-shaped holder. The metastable zone width of $\Delta T_{\text{met}} \approx 12$ °C was determined as the maximum supercooling temperature at which no nucleation occurred on the platinum surface over a 20-h period.

Fluxes 0.1 kg in mass were prepared at $T = 1000$ °C in a cylindrical platinum crucible ($D = 50$ mm, $H = 60$ mm) by melting oxides (Bi_2O_3 , MoO_3 , B_2O_3 , Sm_2O_3 , Fe_2O_3 , Al_2O_3) in a ratio determined using the above formula. The crucible was placed in a furnace where the temperature was reduced from the crucible bottom at a vertical gradient of 1–2 °C/cm. The flux was homogenized at $T = 1000$ °C for 24 h. The flux was stirred to maintain homogeneity.

Single crystals were grown in two stages. First, small crystals about 1 mm in size were grown through spontaneous crystallization at $T = T_{\text{sat}} - (15\text{--}20)$ °C. They were rapidly cooled after removal from the flux. In the next stage, crystals were grown on the seeds. For this, the Pt ring-shaped holder with 10–12 visual quality seeds was immersed in the flux at $T = T_{\text{sat}} + 7$ °C and a reversible rotation with a period of 1 min at $\omega = 30$ rpm was turned on. After 5 min, the temperature was reduced to $T = T_{\text{sat}} - 7$ °C. Then, the temperature was gradually reduced by 1–2 °C per day so that the crystal growth rate did not exceed 1 mm per day. Growth was completed within 3–7 days. The ring was lifted above the surface of the flux and cooled to room temperature at a rate of no more than 100 °C/h. Crystals of about 5–7 mm in size were produced via this process.

The flux was replenished with crystal-forming oxides and used repeatedly. After correcting the flux composition, $\text{SmFe}_{3-y}\text{Al}_y(\text{BO}_3)_4$ crystals with stoichiometries of $y = 0$, 0.05, 0.1, 0.15, and 0.2 were sequentially grown.

2.2. Elemental Analysis

Qualitative elemental analysis of single crystals grown using different contents of Al and a single crystal grown without Al was performed using energy-dispersive X-ray fluorescence using Orbis PC Micro-XRF Analyzer in a vacuum of 0.5 Torr. The accelerating voltage was 40 kV, the beam size was 1 mm, and the amplification time was 12.8 ms. Lines of low intensity corresponding to Al atoms were revealed in the spectra of the crystals grown in the presence of Al_2O_3 . Additionally, low-intensity lines corresponding to Bi atoms were observed for all the crystals.

Quantitative elemental analysis of $\text{Sm}_{1-x}\text{Bi}_x\text{Fe}_{3-y}\text{Al}_y(\text{BO}_3)_4$ crystals was performed using energy-dispersive X-ray elemental analysis using an FEI Quanta 200 3D Dual Beam scanning electron microscope equipped with an EDAX microanalyzer. The accelerating voltage was 20 kV. Several measurements were taken at the same mode for different $\text{Sm}_{1-x}\text{Bi}_x\text{Fe}_{3-y}\text{Al}_y(\text{BO}_3)_4$ samples. Sm:Bi and Fe:Al atomic ratios were estimated based on At.%, assuming that Bi atoms partially substitute Sm atoms, and Al atoms partially substitute Fe atoms. The Bi content was about $x = 5\text{--}7\%$ relative to Sm in all the samples, which is consistent with results obtained previously for Bi-containing rare-earth iron borates [15]. The aluminium content was $y = 0, 0.07(1), 0.17(1), 0.25(1), 0.28(1)$ relative to Fe.

Elemental mapping was performed for the $\text{Sm}_{1-x}\text{Bi}_x\text{Fe}_{3-y}\text{Al}_y(\text{BO}_3)_4$ sample with the highest aluminium content ($y = 0.28(1)$) following EDX elemental analysis in an FEI Osiris transmission electron microscope with a HAADF (high-angle annular dark-field) X-ray detector and an EDX analysis block Bruker SuperX at an accelerating voltage of 200 kV. For these measurements, a single crystal was ground in a mortar and the samples were placed on a carbon-coated copper grid. Based on the mapping results, element distribution was uniform for different samples; low-content Bi and Al atoms were also distributed uniformly in the crystal (Figure 1).

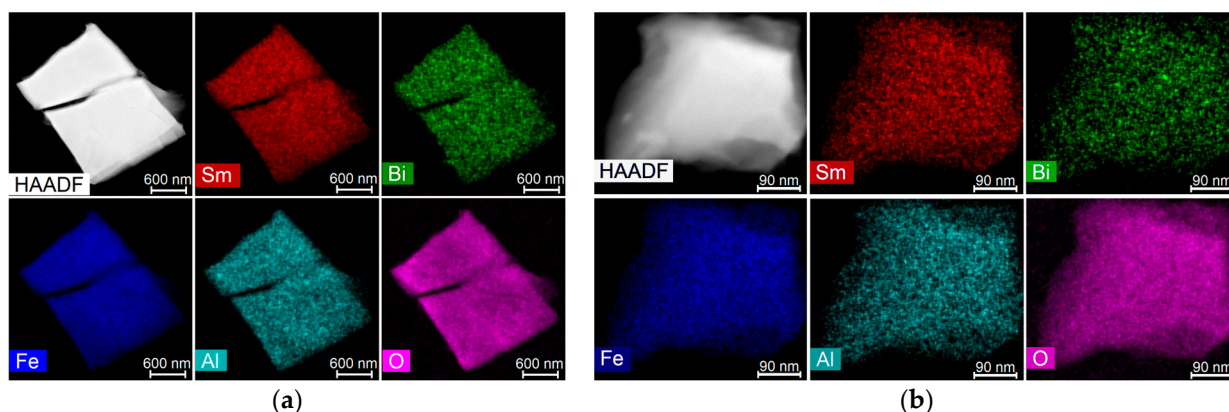
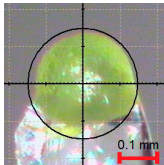
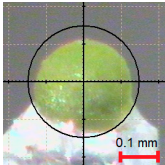
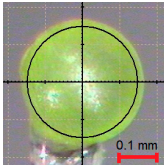
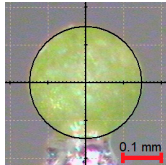
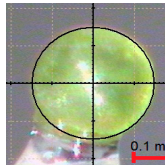


Figure 1. Distribution of chemical elements in $\text{Sm}_{0.93}\text{Bi}_{0.07}\text{Fe}_{2.72}\text{Al}_{0.28}(\text{BO}_3)_4$ single crystals of different sizes: (a) 600 nm and (b) 90 nm.

2.3. Single Crystal X-ray Diffraction

X-ray diffraction (XRD) datasets of $\text{Sm}_{1-x}\text{Bi}_x\text{Fe}_{3-y}\text{Al}_y(\text{BO}_3)_4$ single crystals were obtained at 293 K using CCD Xcalibur EOS S2 diffractometer (Rigaku Oxford Diffraction) with a Cobra Plus temperature attachment (Oxford Cryosystems). Samples were prepared by chipping off the single crystals and generating spherical shapes using airflow in an abrasive chamber in order to correctly account for the absorption of the X-rays. The diameters of the samples were 0.26–0.34 mm. Experimental details are given in Table 2. Crystal structure files CIF S1–S5 are given in Supplementary Materials.

Table 2. Experimental details and structural refinement parameters of $\text{Sm}_{1-x}\text{Bi}_x\text{Fe}_{3-y}\text{Al}_y(\text{BO}_3)_4$ single crystals at 293 K.

Chemical Formula	$\text{Sm}_{0.95}\text{Bi}_{0.05}\text{Fe}_3(\text{BO}_3)_4$	$\text{Sm}_{0.93}\text{Bi}_{0.07}\text{Fe}_{2.93}\text{Al}_{0.07}(\text{BO}_3)_4$	$\text{Sm}_{0.95}\text{Bi}_{0.05}\text{Fe}_{2.83}\text{Al}_{0.17}(\text{BO}_3)_4$	$\text{Sm}_{0.95}\text{Bi}_{0.05}\text{Fe}_{2.75}\text{Al}_{0.25}(\text{BO}_3)_4$	$\text{Sm}_{0.93}\text{Bi}_{0.07}\text{Fe}_{2.72}\text{Al}_{0.28}(\text{BO}_3)_4$
CSD	2,271,136	2,271,135	2,271,124	2,271,134	2,271,125
Crystal shape and colour					
Crystal data					
M_r	556.1	555.2	551.2	548.8	549.2
a, c (Å)	9.5650 (1), 7.5869 (1)	9.5595 (1), 7.5816 (1)	9.5534 (1), 7.5767 (1)	9.5435 (1), 7.5628 (1)	9.5329 (1), 7.5553 (1)
V (Å ³)	601.13 (1)	600.02 (1)	598.86 (1)	596.53 (1)	594.61 (1)
D_x (Mg m ⁻³)	4.608	4.610	4.585	4.583	4.601
μ (mm ⁻¹)	13.35	13.56	13.13	13.05	13.34
Crystal radius (mm)	0.14	0.12	0.17	0.15	0.15
No. of measured/ independent/ observed [$I > 3\sigma(I)$] reflections	20,702/2773/2773	20,709/ 2697/2696	20,631/2744/2744	20,549/2670/2670	20,486/2744/2743
R_{int}	0.027	0.027	0.034	0.029	0.028
$(\sin \theta / \lambda)_{\text{max}}$ (Å ⁻¹)	1.355	1.355	1.356	1.356	1.355
Refinement					
$R[F^2 > 2\sigma(F^2)], wR(F^2), S$	0.011, 0.015, 1.01	0.012, 0.015, 1.01	0.012, 0.017, 1.02	0.012, 0.016, 1.00	0.011, 0.016, 1.03
$\Delta\rho_{\text{max}}, \Delta\rho_{\text{min}}$ (e Å ⁻³)	0.84, -0.88	0.79, -0.90	1.49, -0.54	1.15, -0.51	0.70, -0.86
Absolute structure parameter	0.480 (4)	0.900 (4)	0.779 (5)	0.993 (4)	0.475 (4)

For all structures: trigonal, $R32$, $Z = 3$. Crystal shape: sphere (light green). Experiments were carried out at 293 K with Mo $K\alpha$ radiation using an Xcalibur, EosS2 with high theta cut. Data collection used ω scans. Absorption correction was performed for a Spherical shape in Jana2006. Refinement (36 parameters) was carried out on F .

Temperature dependencies of the unit-cell parameters a , b , and c , and the volume of $\text{Sm}_{1-x}\text{Bi}_x\text{Fe}_{3-y}\text{Al}_y(\text{BO}_3)_4$ single crystals with the highest aluminium content, $y = 0.28$ (1), were measured at temperatures of 85–500 K using Rigaku XtaLAB Synergy-DW (Rigaku Oxford Diffraction) diffractometer with a rotating anode ($\text{MoK}\alpha$ -radiation) and a Rigaku HyPix-Arc 150° detector. The temperature was set using a flow of nitrogen gas via a Cobra Plus temperature attachment (Oxford Cryosystems). The chipped single crystals of size 0.03–0.06 mm were glued to the glass fibre using epoxy resin and used for measurement. An experimental strategy 20 min in duration was conducted, with at least 60 min between experiments.

Complete X-ray diffraction datasets of $\text{Sm}_{1-x}\text{Bi}_x\text{Fe}_{3-y}\text{Al}_y(\text{BO}_3)_4$ with an aluminium content of $y = 0.28$ (1) were obtained at temperatures of 25, 30, 35, 40, 50, 60, 70, and 80 K (helium gas flow) and 110, 150, 220, and 293 K (nitrogen gas flow) using Rigaku XtaLAB Synergy-DW (Rigaku Oxford Diffraction) diffractometer and N-Helix temperature attachment (Oxford Cryosystems). A single crystal with an irregular shape and a size of 0.06–0.14 mm was used. The experimental strategy, which ensured the completeness of the measurements, was 1 h 20 min in duration. The time between experiments was at least 10 min for crystal temperature stabilization. The experimental details are given in Table 3. Crystal structure files CIF S6–S17 are given in Supplementary Materials.

Table 3. Experimental details and structural refinement parameters of $\text{Sm}_{0.93}\text{Bi}_{0.07}\text{Fe}_{2.72}\text{Al}_{0.28}(\text{BO}_3)_4$ single crystal at selected temperatures in the 25–293 K range.

Crystal Data					
Temperature (K)	25	40	80	110	293
CSD	2,271,133	2,271,137	2,271,128	2,271,139	2,271,129
a, c (Å)	9.5430 (1), 7.5634 (1)	9.5438 (1), 7.5616 (1)	9.5444 (1), 7.5601 (1)	9.5450 (1), 7.5598 (1)	9.5452 (1), 7.5680 (1)
V (Å ³)	596.51 (1)	596.47 (1)	596.42 (1)	596.48 (1)	597.15 (1)
D_x (Mg m ⁻³)	4.586	4.586	4.587	4.586	4.581
μ (mm ⁻¹)	13.29	13.29	13.30	13.29	13.28
No. of measured/ independent/ observed [$I > 3\sigma(I)$] reflections	74,155/ 2822/ 2820	74,207/ 2824/ 2823	74,222/ 2823/ 2820	74,140/ 2824/ 2818	73,951/ 2825/ 2750
R_{int}	0.085	0.072	0.076	0.077	0.098
$(\sin \theta / \lambda)_{\text{max}}$ (Å ⁻¹)	1.362	1.363	1.363	1.363	1.362
Refinement					
$R[F^2 > 2\sigma(F^2)],$ $wR(F^2), S$	0.016, 0.038, 1.01	0.015, 0.033, 1.02	0.015, 0.034, 1.02	0.016, 0.038, 1.00	0.022, 0.046, 1.00
$\Delta\rho_{\text{max}}, \Delta\rho_{\text{min}}$ (e Å ⁻³)	1.86, -1.63	0.96, -1.10	1.06, -1.53	0.94, -1.34	1.13, -0.76
Absolute structure parameter	0.041 (5)	0.032 (5)	0.030 (5)	0.035 (5)	0.044 (7)

For all structures: $M_r = 549.2$, trigonal, $R32$, $Z = 3$. Crystal shape: irregular (light green). Crystal size: $0.14 \times 0.09 \times 0.06$ mm. Experiments were carried out using $\text{Mo K}\alpha$ radiation with an XtaLAB Synergy-DW system, HyPix-Arc 150. Data collection used ω scans. Gaussian, *CrysAlis PRO* 1.171.42.63a (Rigaku Oxford Diffraction, 2022). Absorption was corrected using numerical methods: absorption correction was based on Gaussian integration over a multifaceted crystal model and empirical absorption correction used spherical harmonics implemented in SCALE3 ABSPACK scaling algorithm. Refinement (36 parameters) was carried out on F^2 .

There was a systematic difference between the unit-cell parameters a , b , and c and the volume obtained using Cobra Plus and N-Helix temperature attachments that was considered based on the shift in Cobra Plus dependencies to N-Helix dependencies using a coefficient as described in [40].

Analysis of the three-dimensional distribution of reflection peaks, unit-cell finding, and integration of diffraction intensities was performed using *CrysAlisPro* software [41].

The structures were refined using the least-squares method and anisotropic approximation of atomic displacements using the Jana2006 program [42].

The trigonal unit cell (hexagonal setting) was chosen for all the crystals based on the analysis of three-dimensional diffraction peak distribution (Tables 2 and 3). More than 97% (3D peak hunting procedure [41]) or 73% (Smart peak hunting procedure for datasets obtained using CCD detector [41]) of observed reflections were indexed in the chosen trigonal unit cells for all the samples. Reflection tails and lambda-half reflections were deleted for accurate indexation [41] and there were no additional phases found. In the case of a forced search for a monoclinic unit cell of $\text{SmAl}_3(\text{BO}_3)_4$ [21], the same quantity of observed reflections was indexed in the unit cell. However, the regular absence of reflections in the reciprocal lattice points in the case of a monoclinic unit cell indicated the wrong choice of the monoclinic unit cell for the crystals studied in the present work (Appendix A).

For datasets obtained using the Synergy-DW diffractometer, both empirical and numerical correction for a multifaceted crystal were performed during finalization in CrysAlisPro. For datasets obtained using Xcalibur EOS S2, empirical correction was performed in CrysAlisPro and correction for a spherical shape was performed in Jana2006.

It was confirmed that Bi atoms partially substitute Sm atoms in their positions, and Al atoms partially substitute Fe atoms, consistent with Shannon ionic radii (0.958 Å for Sm^{3+} and 1.03 Å for Bi^{3+} with the coordination number VI; 0.645 Å for high-spin Fe^{3+} and 0.535 Å for Al^{3+} with the coordination number VI) [43,44]. Sm:Bi and Fe:Al ratios in the final chemical formulas (Table 2) were based both on elemental analysis and XRD refinement. Splitting Sm:Bi and Fe:Al positions did not significantly influence refinement disagreement factors and residual electron density, therefore identical coordinates and anisotropic displacement parameters (ADPs) for Sm and Bi, and for Fe and Al were used, and the sums of overall occupancy factors were constrained.

Absolute configuration was considered by refining the ratio of the volumes of the racemic twin components (Flack parameter) [45]. Taking into account the extinction effect, the best Becker–Coppens model [46,47] was selected for each of the experiments where the orientation of the mosaic blocks was distributed according to the Lorentz law (type 1).

Coefficients and characteristic surfaces of thermal expansion tensor were obtained based on the temperature dependencies of unit-cell parameters using the ThetaToTensor (TTT) program [48]. Unit cell parameter a was fitted using polynomials of the second degree and parameter c was best fitted using the third-degree polynomial over the temperature range 25–500 K. Fitting parameters a and c using different second-degree polynomials within the temperature intervals led to similar shapes of thermal expansion figures in the temperature range 25–500 K but with more complicated temperature dependencies of thermal expansion eigenvalues, which was considered unreliable. Thermal expansion coefficient eigenvalues are given in Table 4.

Table 4. Eigenvalues of thermal expansion tensor of $\text{Sm}_{0.93}\text{Bi}_{0.07}\text{Fe}_{2.72}\text{Al}_{0.28}(\text{BO}_3)_4$ at selected temperatures (multiplied by 10^6 , K).

Coefficient α	25	50	100	120	140	293	400	500
$\alpha_{11}(=\alpha_{22}, \alpha_a, \alpha_b)$	−0.9 (2)	−0.7 (2)	−0.20 (12)	0.0 (1)	0.2 (1)	1.55 (6)	2.53 (12)	3.4 (2)
$\alpha_{33}(=\alpha_c)$	−8.2 (5)	−5.2 (4)	0.0 (2)	1.82 (13)	3.48 (11)	11.23 (14)	11.5 (2)	7.8 (6)
$\mu_{a1} = \angle \alpha_{11,a} (^\circ)$	30	30	30	30	30	30	30	30
α_V	−10 (1)	−7 (1)	−0.4 (3)	1.82 (13)	3.8 (2)	14.3 (2)	16.5 (3)	15 (1)

Based on the values of the equivalent isotropic atomic displacement parameters U_{eq} obtained for atoms in the $\text{Sm}_{0.93}\text{Bi}_{0.07}\text{Fe}_{2.72}\text{Al}_{0.28}(\text{BO}_3)_4$ structure at 12 temperatures, the characteristic Debye temperature (T_D) and Einstein temperature (T_E) were calculated (Table 5) using the models described in [49]. Model $U_{\text{eq}}(T)$ dependencies in both approxi-

mations were obtained. Effective relative atomic masses for (Sm,Bi) and (Fe,Al) atoms were used for the calculations. The modelling agreement factors are given in Table 5.

Table 5. Characteristic temperatures and static atomic displacements in $\text{Sm}_{0.93}\text{Bi}_{0.07}\text{Fe}_{2.72}\text{Al}_{0.28}(\text{BO}_3)_4$. Debye T_D and Einstein T_E characteristic temperatures, their difference, ΔT_{DE} , values of zero-point oscillations, $\langle u^2 \rangle_{\text{zero}}$ and $\langle u^2 \rangle_{\text{shift}}$ ($\langle u^2 \rangle_{\text{static}} = \langle u^2 \rangle_{\text{zero}} + \langle u^2 \rangle_{\text{shift}}$) for atoms in the $\text{Sm}_{0.93}\text{Bi}_{0.07}\text{Fe}_{2.72}\text{Al}_{0.28}(\text{BO}_3)_4$ structure, and R -factors of model refinement. The top-line $\langle u^2 \rangle_{\text{zero}}$ and $\langle u^2 \rangle_{\text{shift}}$ is the Einstein approximation and the bottom-line is the Debye approximation.

	T_E , K	T_D , K	ΔT_{DE}	$\langle u^2 \rangle_{\text{zero}} \text{ \AA}^2$	$\langle u^2 \rangle_{\text{shift}} \text{ \AA}^2$	R , %
(Sm,Bi)	118 (1)	205 (1)	87	0.001333	0.00143 (2)	0.95
				0.001148	0.00148 (2)	0.73
(Fe,Al)	245 (2)	436 (2)	191	0.001865	0.00075 (3)	1.32
				0.001572	0.00094 (2)	0.75
O1	385 (7)	708 (9)	323	0.003214	0.00052 (11)	2.63
				0.003331	0.00111 (7)	1.46
O2	300 (6)	540 (6)	240	0.005047	0.0015 (2)	2.97
				0.004208	0.00210 (10)	1.62
O3	342 (5)	622 (5)	280	0.004429	0.00032 (12)	2.69
				0.003656	0.00092 (6)	1.2
B1	518 (21)	983 (34)	465	0.004336	−0.0002 (2)	4.03
				0.003423	0.0006 (2)	3.09
B2	461 (13)	861 (16)	400	0.004869	−0.0006 (2)	3.94
				0.003908	0.0003 (1)	2.27

Three-dimensional visualization of electron density distribution was additionally obtained using the maximum entropy method (MEM) implemented in the Dysnomia software [50]. Calculations were performed based only on observed structure amplitudes, F_{obs} , using the lowest possible $P1$ symmetry in order not to restrain electron density map by symmetry laws and to get a more detailed distribution.

Quantitative measurements of coordination polyhedra distortions from ideal symmetry were performed using the Polynator program [51] by minimizing the squares of vertex deviations.

3. Results and Discussion

3.1. Temperature Dependencies of Unit-Cell Parameters

Unit cell parameters of $\text{Sm}_{1-x}\text{Bi}_x\text{Fe}_{3-y}\text{Al}_y(\text{BO}_3)_4$ ($x = 0.05\text{--}0.07$, $y = 0\text{--}0.28$) single crystals (Table 2) decreased with an increase in aluminium content from 0 to 0.28. This agrees with the difference in Shannon ionic radii [43,44].

There were no structural phase transitions in $\text{Sm}_{0.93}\text{Bi}_{0.07}\text{Fe}_{2.72}\text{Al}_{0.28}(\text{BO}_3)_4$ in the 25–500 K temperature range based on lattice parameter dependencies (Figure 2a). Temperature dependencies of $\text{Sm}_{0.93}\text{Bi}_{0.07}\text{Fe}_{2.72}\text{Al}_{0.28}(\text{BO}_3)_4$ unit-cell parameters (Figure 2a) demonstrate similar behaviours to those of samarium and neodymium iron borates, which do not have structural phase transitions from the $R32$ space group at low temperatures but demonstrate magnetic ordering below $T_N = 32\text{--}33$ K [32,40].

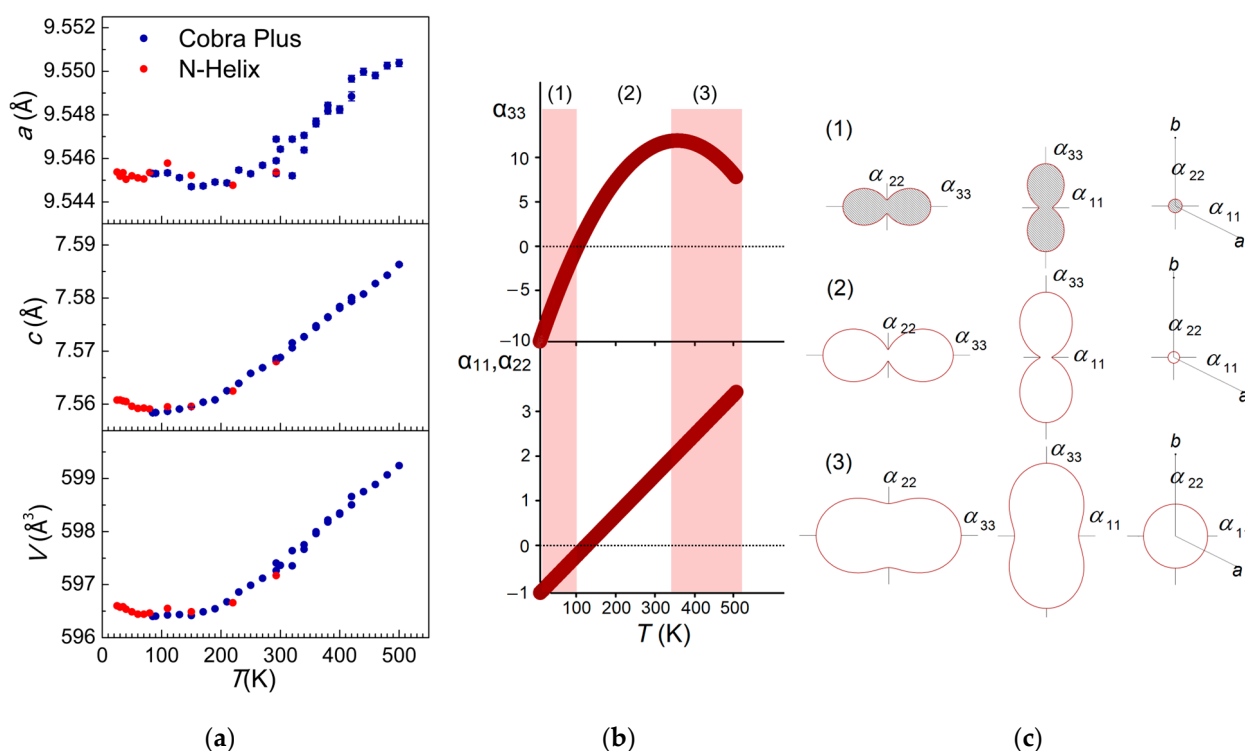


Figure 2. (a) Temperature dependence of unit-cell parameters a and c , and volume V of $\text{Sm}_{0.93}\text{Bi}_{0.07}\text{Fe}_{2.72}\text{Al}_{0.28}(\text{BO}_3)_4$ in the 25–500 K temperature range. Errors are smaller than dot size; (b) Temperature dependence of thermal expansion eigenvalues α_{33} in the c direction and $\alpha_{11} = \alpha_{22}$ in the ab plane based on unit-cell measurements. Three different intervals (1), (2), (3) are shown; (c) General view of thermal expansion figure projections in the $\alpha_{11}, \alpha_{22}, \alpha_{33}$ directions. Example figures of three different temperature intervals are shown. All coefficients in (1) are negative, while those in (2) and (3) are positive.

Unit-cell parameter c undergoes the most pronounced change over the 25–500 K temperature range (Figure 2a): Between 25 K and 85 K it decreases by about 0.002 Å as the temperature rises, and after that it increases steadily by about 0.028 Å from 85 K to 500 K. Unit-cell parameter a varies by no more than 0.0007 Å between 25 and 110 K and then slightly increases by about 0.006 Å from 110 K to 500 K. Unit-cell volume demonstrates the effect of negative thermal expansion, reflecting the behaviour of parameter c . Between 25 K and 85 K, the volume decreases by about 0.1 Å³ and then increases by about 2.8 Å³ (Figure 2a). Such effects of negative thermal expansion were discovered in rare-earth iron borates in both space groups $R32$ and $P3_121$, and were associated with an increase in Fe–Fe intrachain distances and Fe–O–Fe angles in chains along the c -axis formed by FeO_6 distorted octahedra [15].

This effect on $\text{Sm}_{0.93}\text{Bi}_{0.07}\text{Fe}_{2.72}\text{Al}_{0.28}(\text{BO}_3)_4$ was additionally demonstrated by modelling the thermal expansion coefficient based on measured unit-cell parameters (Figure 2b,c, and Figure 3). It can be seen that the main changes in eigenvalues of the tensor appear in the c -axis direction (coefficient α_{33} —Figures 2c and 3, Table 4). Below 100 K, all coefficients— $\alpha_a, \alpha_b, \alpha_c$ and α_V —are negative and negative thermal expansion (contraction) is observed principally in the c direction (Figure 3, Table 4). Contraction is more pronounced at lower temperatures and approaches zero at about 100 K. The thermal expansion coefficient becomes positive in the c direction at about 100 K and in the ab direction at about 120 K (Figure 2b, Table 4). At higher temperatures closer to 500 K, expansion in the ab plane (α_{11}, α_{22}) begins to compete with expansion in the c direction (α_{33}) and the thermal expansion figure becomes closer to isotropic (Figures 2c and 3).

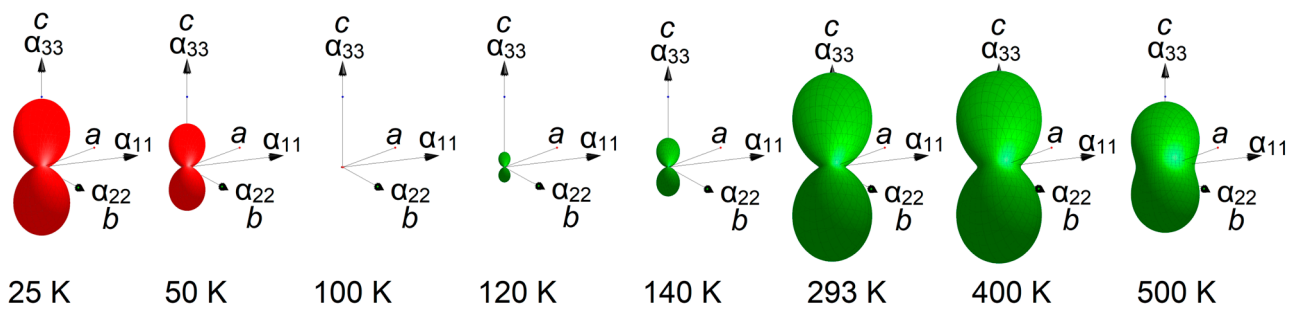


Figure 3. Transformation of the 3D characteristic surface of thermal expansion tensor depending on the temperature. Red and green colours correspond to negative and positive eigenvalues, respectively.

3.2. Crystal Structure of $\text{Sm}_{1-x}\text{Bi}_x\text{Fe}_{3-y}\text{Al}_y(\text{BO}_3)_4$ at Room Temperature

Structures of $\text{Sm}_{1-x}\text{Bi}_x\text{Fe}_{3-y}\text{Al}_y(\text{BO}_3)_4$ ($x = 0.05\text{--}0.07$, $y = 0\text{--}0.28$) single crystals were refined in trigonal $R\bar{3}2$ space group, $Z = 3$ (Table 2, Figure 4). Detailed descriptions of the crystal structures of rare-earth iron borates in this space group can be found in [14,15,32,40,52].

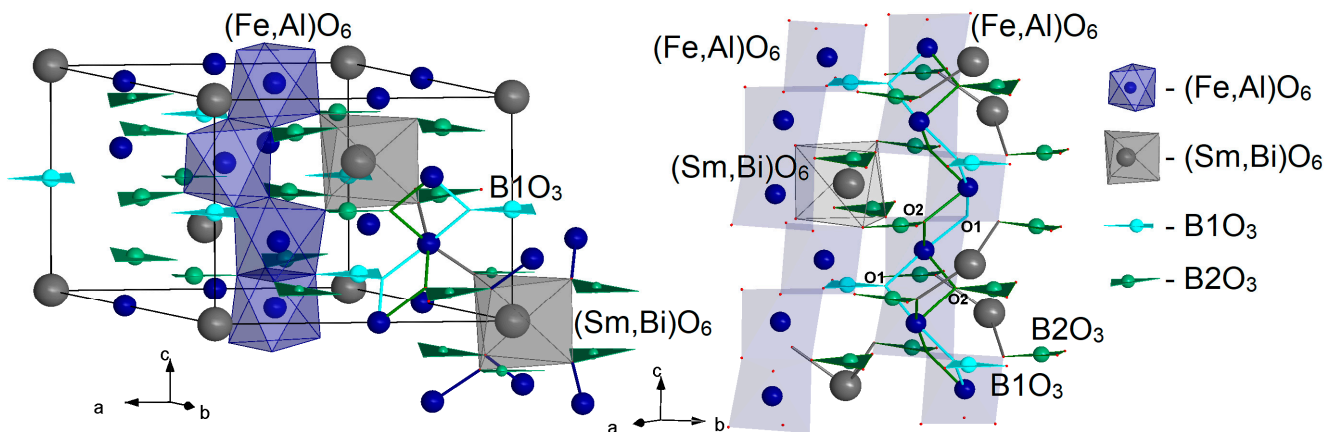


Figure 4. Crystal structure of $\text{Sm}_{0.93}\text{Bi}_{0.07}\text{Fe}_{2.72}\text{Al}_{0.28}(\text{BO}_3)_4$. Bonding of $(\text{Sm,Bi})\text{O}_6$ distorted prisms, $(\text{Fe,Al})\text{O}_6$ distorted octahedra, two types of BO_3 triangles, as well as helicoidal chains of $(\text{Fe,Al})\text{O}_6$ directed along the c -axis are shown. Unit cells are highlighted using black lines. Angles in $(\text{Fe,Al})\text{--O1}\text{--}(\text{Fe,Al})$ are shown in turquoise-blue and angles in $(\text{Fe,Al})\text{--O2}\text{--}(\text{Fe,Al})$ are shown in green. O1 oxygen atoms are vertices of equilateral triangle B1O_3 and O2 are vertices of isosceles triangle B2O_3 .

There is one Wyckoff atomic position ($3a$) for (Sm,Bi) atoms, one ($9d$) position for (Fe,Al) atoms, two positions for boron atoms [B1 ($3b$) and B2 ($9e$)], and three positions for oxygen atoms [O1($9e$), O2($9e$), O3($18f$)] (Figure 4). There are layers of (Sm,Bi) and (Fe,Al) atoms, which alternate in the c -axis direction with layers of two types of BO_3 triangles. Equilateral triangle B1O_3 is parallel to the ab plane, while the isosceles triangle B2O_3 deviates from it slightly. (Sm,Bi) atoms are in trigonal $(\text{Sm,Bi})\text{O}_6$ prisms whose bases are slightly rotated relative to each other. (Fe,Al) atoms are in distorted $(\text{Fe,Al})\text{O}_6$ octahedra connected by the edges and form helicoidal chains along the c -axis. B1O_3 triangles are connected only to three $(\text{Fe,Al})\text{O}_6$ chains, whereas B2O_3 triangles are connected both to $(\text{Fe,Al})\text{O}_6$ octahedra and $(\text{Sm,Bi})\text{O}_6$ prisms. $(\text{Sm,Bi})\text{O}_6$ prisms are connected to three $(\text{Fe,Al})\text{O}_6$ chains directly or through B2O_3 triangles (Figure 4).

The characters of electron density distributions are similar for $\text{Sm}_{1-x}\text{Bi}_x\text{Fe}_{3-y}\text{Al}_y(\text{BO}_3)_4$ single crystals with $y = 0, 0.07, 0.17, 0.25$ and 0.28 (Figure 5). The electron density distribution maps do not show significant anisotropy of the (Sm,Bi) and (Fe,Al) positions, which, together with low values of structure refinement factors and values of residual electron density, $\Delta\rho_{\text{max}}$ and $\Delta\rho_{\text{min}}$, indicates a low degree of local disordering at these positions. The highest values of residual electron density not accounted for (Table 2) are spread at

distances of 0.28–1.03 Å from the (Sm,Bi) position. This residual density can originate from the configuration of electron shells or can be a result of features of mathematical apparatus used in the least squares refinement method [53,54].

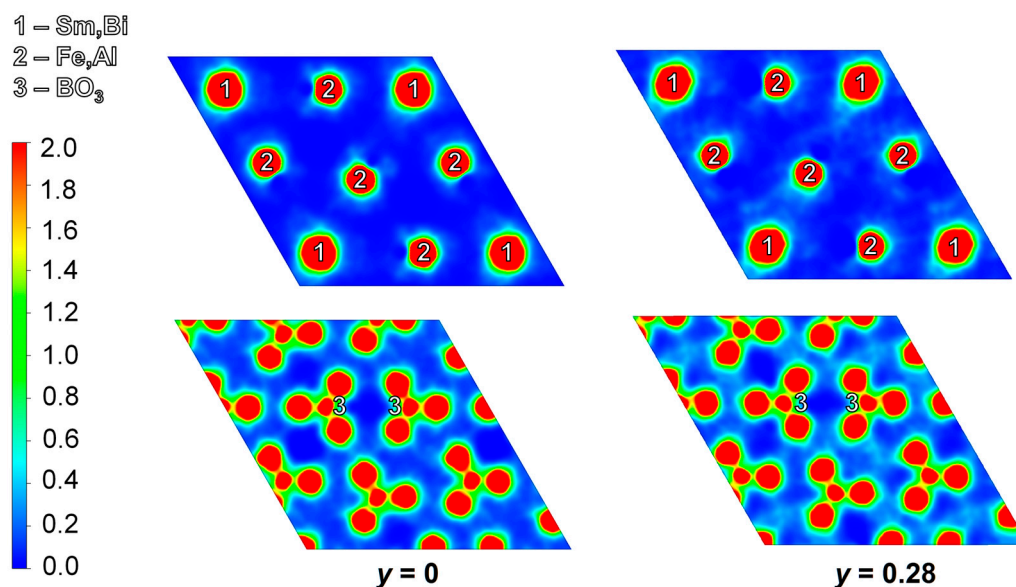


Figure 5. Electron density distribution in $\text{Sm}_{0.95}\text{Bi}_{0.05}\text{Fe}_3(\text{BO}_3)_4$ ($y = 0$) and $\text{Sm}_{0.93}\text{Bi}_{0.07}\text{Fe}_{2.72}\text{Al}_{0.28}(\text{BO}_3)_4$ ($y = 0.28$) at 293 K built using the maximum entropy method (MEM). Sections parallel to the ab plane are built in a plane going through atoms 1—(Sm,Bi) and 2—(Fe,Al) and in a plane going through 3— BO_3 triangles. Electron density distribution is shown using a colour gradient: red corresponds to maximum saturation (rate = 2 \AA^{-3}) and blue corresponds to minimum saturation (rate = 0).

Analysis of the Flack parameter (Table 2) demonstrated that $\text{Sm}_{1-x}\text{Bi}_x\text{Fe}_{3-y}\text{Al}_y(\text{BO}_3)_4$ single crystals with $y = 0, 0.07, 0.17, 0.25,$ and 0.28 can be merohedral racemic twins (for two components of which perfect overlapping of reflections is observed, and twin operation is inversion). Two of the crystals ($y = 0$ and 0.28) were merohedral racemic twins with almost equal ratios of opposite twin components. The ratios of the two twin components of the sample with $y = 0.17$ were unequal. Two other samples ($y = 0.07, 0.25$) were almost monodomain (Table 2). Therefore, $\text{Sm}_{1-x}\text{Bi}_x\text{Fe}_{3-y}\text{Al}_y(\text{BO}_3)_4$ single crystals have different absolute configurations that have to be taken into account when studying their physical properties.

Relative atomic coordinates of samples with absolute configuration parameter Flack > 0.5 (opposite chirality to the modelled one) were not inverted for the convenience of structure comparison. The single crystal chosen for the temperature XRD experiments was almost monodomain (Flack ≈ 0 , Table 3).

A slight decrease of $\approx 0.004 \text{ \AA}$ in (Sm,Bi)– O_3 interatomic distances in a distorted trigonal (Sm,Bi) O_6 prism occurs as the content of aluminium increases from 0 to 0.28 (Figure 6a). The decrease in distances from the (Sm,Bi) atom to the more distant oxygen atom O2(9e) is $\approx 0.011 \text{ \AA}$. O_2 atoms connect B_2O_3 triangles with iron chains (Figure 4). They have a special role in structural rearrangement in rare-earth iron borates with ionic radii smaller than that of Sm having $R32 \rightarrow P3_121$ structural phase transition. O_2 splits into two independent positions below the structural phase transition temperature; oxygen atoms from one approaches R -atom and influences the paths of exchange bonding [15]. Therefore, a noticeable decrease in (Sm,Bi)– O_2 distance with the inclusion of aluminium atoms could also influence the exchange paths at lower temperatures. There is also a noticeable decrease of $\approx 0.013 \text{ \AA}$ in distances between (Sm,Bi) and (Fe,Al) atoms, which could influence indirect (Sm,Bi)–(Fe,Al) interaction (Figure 6e).

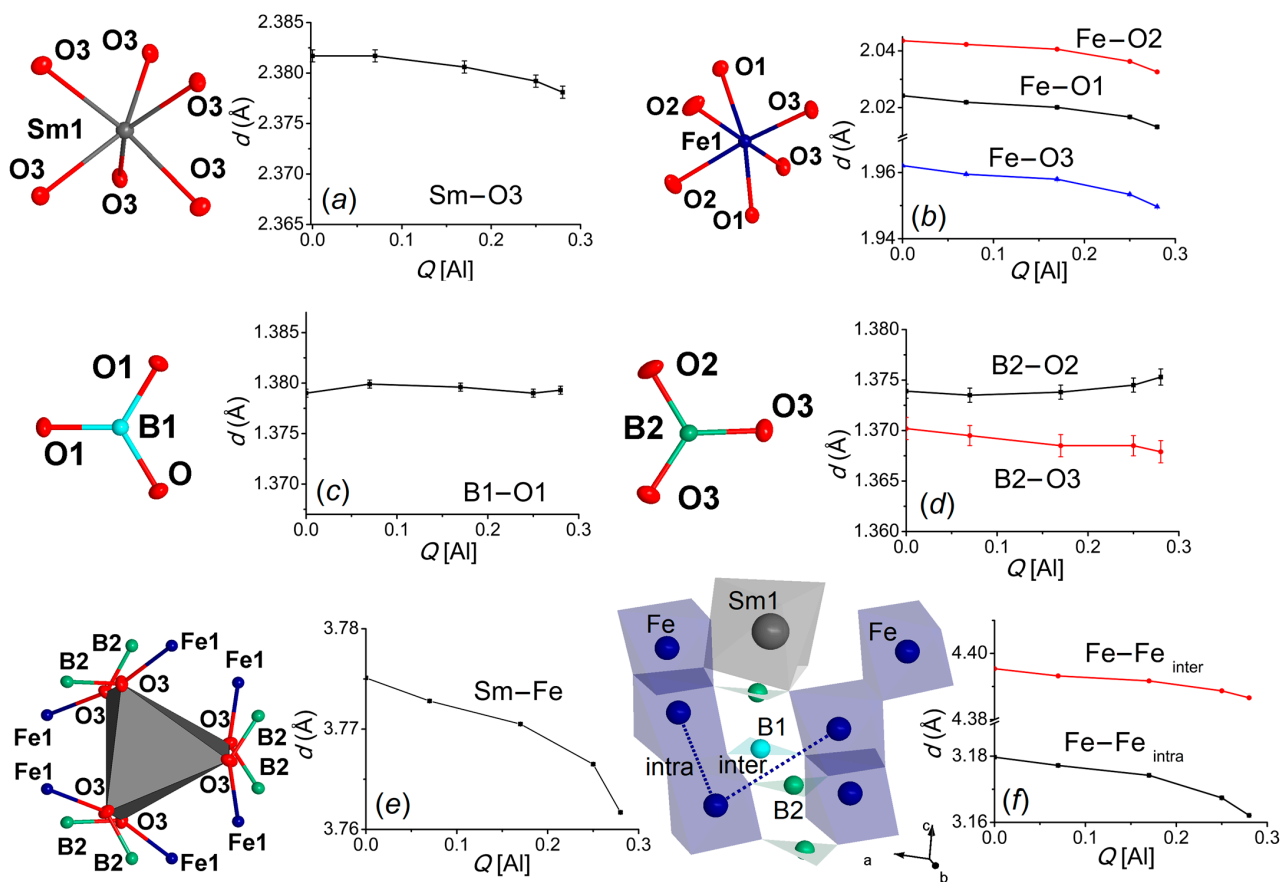


Figure 6. Interatomic distances in the structures of $\text{Sm}_{1-x}\text{Bi}_x\text{Fe}_{3-y}\text{Al}_y(\text{BO}_3)_4$ ($x = 0.05\text{--}0.07$, $y = 0\text{--}0.28$) depending on the aluminium content: (a) (Sm,Bi)–O₃ in distorted trigonal (Sm,Bi)O₆ prism; (b) (Fe,Al)–O in distorted (Fe,Al)O₆ octahedra; (c) B₁–O in B₁O₃ equilateral triangle; (d) B₂–O in B₂O₃ isosceles triangle; (e) (Sm,Bi)–(Fe,Al) closest distances; (f) Distances between atoms in (Fe,Al)–(Fe,Al) chains (intra) and between the closest atoms in different (Fe,Al)–(Fe,Al) chains (inter). For clarity, Bi and Al atoms are not labelled.

(Fe,Al)–O distances in distorted (Fe,Al)O₆ octahedra also decrease with the increase in the content of aluminium (Figure 6b). (Fe,Al)–O distances of different types decrease almost uniformly by $\approx 0.011\text{--}0.012$ Å. (Fe,Al)–(Fe,Al) distances in the same chain decrease by ≈ 0.018 Å with the addition of Al, and the closest distance between two (Fe,Al)–(Fe,Al) chains decreases by ≈ 0.009 Å (Figure 6f).

Boron coordination is the most stable, depending on the aluminium content (Figure 6c,d), similar to the temperature dependence of boron coordination [15]. B₁–O distance varies by no more than ≈ 0.0003 Å, B₂–O₂ distance increases by ≈ 0.0014 Å, and B₂–O₃ distance decreases by ≈ 0.0023 Å with Al addition.

3.3. Crystal Structure of $\text{Sm}_{0.93}\text{Bi}_{0.07}\text{Fe}_{2.72}\text{Al}_{0.28}(\text{BO}_3)_4$ in the 25–293 K Temperature Range

The structure of $\text{Sm}_{0.93}\text{Bi}_{0.07}\text{Fe}_{2.72}\text{Al}_{0.28}(\text{BO}_3)_4$ single crystal was refined in trigonal space group $R\bar{3}2$, $Z = 3$ at all the temperatures studied (Table 3). There were no reflections corresponding to systematic absences.

Interatomic distances were analyzed in $\text{Sm}_{0.93}\text{Bi}_{0.07}\text{Fe}_{2.72}\text{Al}_{0.28}(\text{BO}_3)_4$ depending on temperature. Crystal structural features of $\text{Sm}_{0.93}\text{Bi}_{0.07}\text{Fe}_{2.72}\text{Al}_{0.28}(\text{BO}_3)_4$ in low-temperature regions are of interest since there is a magnetic phase transition below $T_N = 31.93$ (5) K for samarium iron borate [32]. The negative thermal expansion, observed for rare-earth iron borates below 100 K, was accompanied by an increase in Fe–Fe intrachain distances

and Fe–O–Fe angles when the temperature was lowered from 90 K to 25 K; however, this observation needs additional analysis [15].

This distinct behaviour of (Fe,Al)–(Fe,Al) chains is also observed in $\text{Sm}_{0.93}\text{Bi}_{0.07}\text{Fe}_{2.72}\text{Al}_{0.28}(\text{BO}_3)_4$ (Figure 7f,g). Distances between (Fe,Al) atoms in the same chain decrease by $\approx 0.0025 \text{ \AA}$ when the temperature is lowered from 293 K to 150 K, before increasing by $\approx 0.0032 \text{ \AA}$ such that the (Fe,Al)–(Fe,Al) distance at 25 K is higher than the distance at 293 K (Figure 7f). At the same time, the closest distance between different (Fe,Al)–(Fe,Al) chains decreases slowly by $\approx 0.002 \text{ \AA}$ from 293 K to 60 K and then drops by $\approx 0.0027 \text{ \AA}$ from 60 K to 25 K (Figure 7f). The (Fe,Al)–O–(Fe,Al) intrachain angles increased when the temperature dropped below 100 K (Figure 7g).

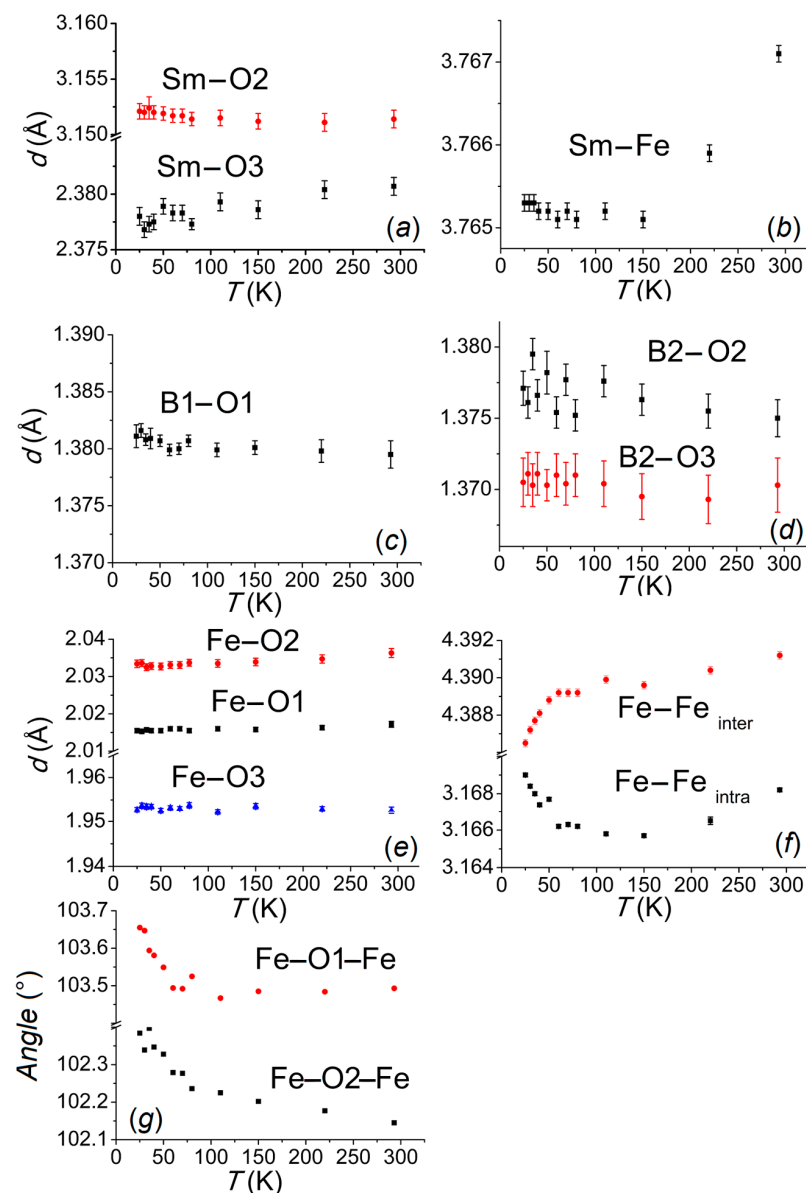


Figure 7. Interatomic distances in $\text{Sm}_{0.93}\text{Bi}_{0.07}\text{Fe}_{2.72}\text{Al}_{0.28}(\text{BO}_3)_4$ depending on the temperature: (a) (Sm,Bi)–O3 in distorted trigonal (Sm,Bi) O_6 prism and (Sm,Bi)–O2 to the more distant oxygen atom; (b) (Sm,Bi)–(Fe,Al) closest distances; (c) B1–O in B1O_3 equilateral triangle; (d) B2–O in B2O_3 isosceles triangle; (e) (Fe,Al)–O in distorted (Fe,Al) O_6 octahedra; (f) Distances between atoms in (Fe,Al)–(Fe,Al) chains (intra) and between the closest atoms in different (Fe,Al)–(Fe,Al) chains (inter); (g) Angles (Fe,Al)–O–(Fe,Al) in the chain. For clarity, Bi and Al atoms are not labelled on the figure.

(Fe,Al)–O1 distance in (Fe,Al)O₆ octahedra decreases by ≈ 0.0019 Å, (Fe,Al)–O2 distance decreases by ≈ 0.0029 Å, and (Fe,Al)–O3 distance does not change by more than ≈ 0.0011 Å (Figure 7e) as the temperature is lowered.

B1–O distance in the B1O₃ triangle increases slightly by ≈ 0.0016 Å, B2–O2 distance in the B2O₃ triangle increases by ≈ 0.004 Å, and B2–O3 distance does not change by more than ≈ 0.0008 Å (Figure 7c,d) as the temperature is lowered. The angle of deviation of B2O₃ from the *ab* plane is equal to $6.3 (1)^\circ$ in the whole 25–293 K temperature range.

The distance between (Sm,Bi) and (Fe,Al) magnetic atoms decreases by ≈ 0.0019 Å as the temperature is lowered from 293 K to 150 K, but does not change by more than ≈ 0.0002 Å as the temperature decreases to 25 K (Figure 7b).

(Sm,Bi)–O3 distance in the (Sm,Bi)O₆ prism decreases by ≈ 0.0018 Å as the temperature is lowered from 293 K to 25 K, but the distance to the more distant oxygen atom O2 in (Sm,Bi)–O2 changes by no more than ≈ 0.0007 Å (Figure 7a).

Therefore, even though no structural phase transition occurs in Sm_{0.93}Bi_{0.07}Fe_{2.72}Al_{0.28}(BO₃)₄ in the 25–293 K temperature range, there are noticeable non-uniform structural changes below 100 K that can precede the appearance of magnetic arrangement.

Figure 8 demonstrates the shifts in the vertices of (Fe,Al)O₆ octahedra (O1, O2, O3) from the ideal positions in the regular octahedron modelled around (Fe,Al) atoms based on both Al content and temperature. The shift in oxygen vertex O2 is the most pronounced across all the Al contents and temperatures analysed, which additionally highlights its role in structural rearrangement. The shift in all the vertexes increases as the temperature reduces in the negative thermal expansion region, another evidence that negative thermal expansion is associated with the rearrangement of (Fe,Al)O₆ chains.

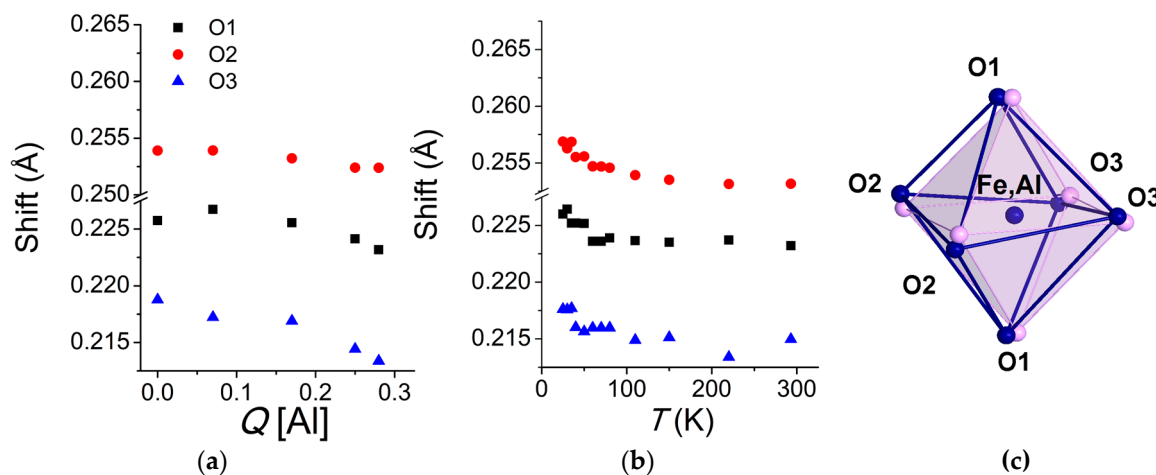


Figure 8. Shift in the vertices of (Fe,Al)O₆ octahedra (O1, O2, O3) from the ideal positions in the regular octahedron modelled around (Fe,Al) atoms: (a) The shift in the structures of Sm_{1-x}Bi_xFe_{3-y}Al_y(BO₃)₄ based on aluminium content ($y = 0-0.28$); (b) The shift in the structure of Sm_{0.93}Bi_{0.07}Fe_{2.72}Al_{0.28}(BO₃)₄ based on temperature; (c) Regular octahedron is shown in pink and (Fe,Al)O₆ octahedron in the Sm_{0.93}Bi_{0.07}Fe_{2.72}Al_{0.28}(BO₃)₄ structure at 25 K is shown in blue.

Change observed in the temperature dependence of (Fe,Al)–(Fe,Al) interchain and intrachain, (Sm,Bi)–(Fe,Al) distances between magnetic ions in the region of negative thermal expansion could lead to the evolution of exchange and super-exchange paths at lower temperatures. The increase in (Fe,Al)–(Fe,Al) intrachain bond lengths at low temperatures could weaken this bond, whereas a decrease in (Fe,Al)–(Fe,Al) interchain distances and unchanged (Sm,Bi)–(Fe,Al) distances at low temperatures could strengthen super-exchange paths between different chains.

However, Sections 3.2 and 3.3 showed that the addition of aluminium atoms had a stronger influence on interatomic distances in Sm_{1-x}Bi_xFe_{3-y}Al_y(BO₃)₄ structures than lowering the temperature from 293 K to 25 K. Thus, growing Sm_{1-x}Bi_xFe_{3-y}Al_y(BO₃)₄ single

crystals using a higher concentration of Al is of interest since a decrease in (Sm,Bi)–(Fe,Al), (Sm,Bi)–O2, and (Fe,Al)–(Fe,Al) distances could influence magnetoelectric properties at low temperatures. Besides that, substituting iron atoms in $R\text{Fe}_3(\text{BO}_3)_4$ structures with $R = \text{Eu}–\text{Er}$ with atoms of other metals could highlight the influence of these atoms on $R32 \rightarrow P3_121$ structural phase transition.

3.4. Atomic Displacement Parameters

Equivalent isotropic parameters U_{eq} of atomic displacements (ADPs) in $\text{Sm}_{0.93}\text{Bi}_{0.07}\text{Fe}_{2.72}\text{Al}_{0.28}(\text{BO}_3)_4$ decrease as the temperature is lowered (Figure 9). Similar to the $(\text{Sm}_{0.93}\text{Bi}_{0.07})\text{Fe}_3(\text{BO}_3)_4$ structure [32], the most steep dependence is that of $U_{\text{eq}}(T)$ for (Sm,Bi) and O2 atoms. At high temperatures, U_{eq} of (Sm,Bi) is higher than U_{eq} of Fe; however, these values approach convergence at 25 K (Figure 9a), which could reflect the exchange interaction difference at high and low temperatures. O2 atoms have the highest value of U_{eq} across the whole temperature range analysed. It is worth noting that the highest U_{eq} of all the atoms in the structures of $\text{NdGa}_3(\text{BO}_3)_4$ ($P3_121$ space group) [55], $\text{NdSc}_3(\text{BO}_3)_4$ [56], and $\text{HoAl}_3(\text{BO}_3)_4$ [57] ($R32$ space group) are of the oxygen atoms corresponding to O2(9e) in the $\text{Sm}_{0.93}\text{Bi}_{0.07}\text{Fe}_{2.72}\text{Al}_{0.28}(\text{BO}_3)_4$ structure (which splits into two independent positions in the $P3_121$ space group).

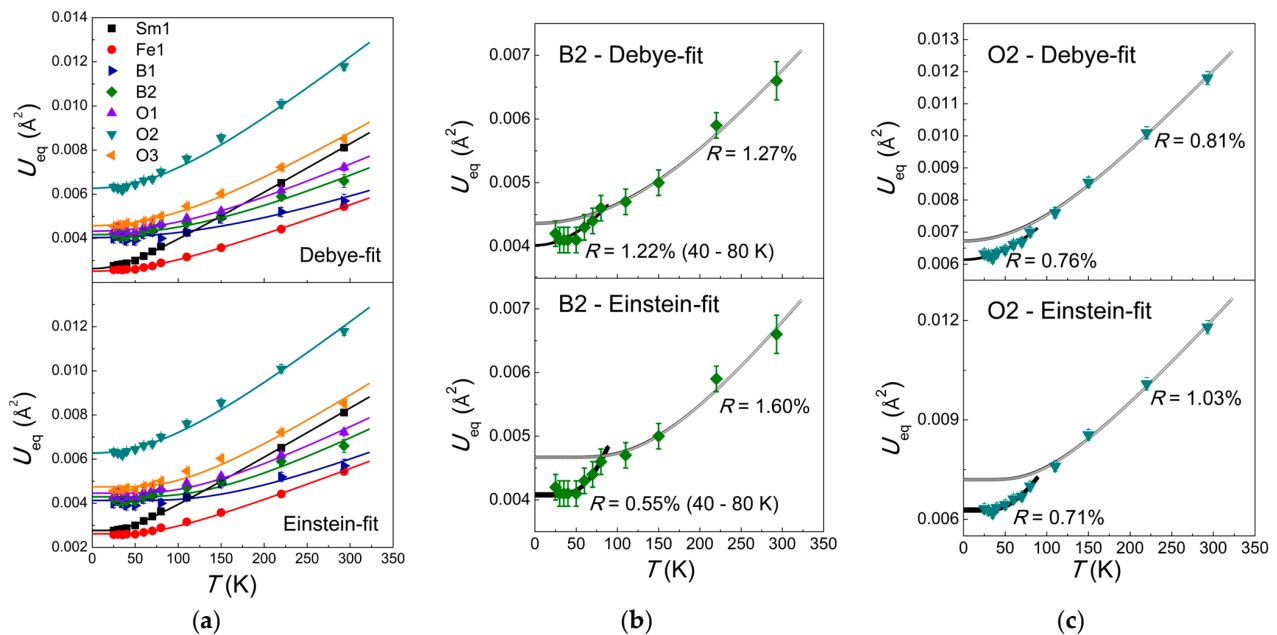


Figure 9. Temperature dependence of equivalent isotropic displacement parameters of atoms in the structure of $\text{Sm}_{0.93}\text{Bi}_{0.07}\text{Fe}_{2.72}\text{Al}_{0.28}(\text{BO}_3)_4$. Experimental XRD values are shown together with the model curves in Debye or Einstein extended approximation: (a) all U_{eq} dependencies are modelled using single curves; (b) U_{eq} of boron atoms B2(9e) are modelled using two curves; (c) U_{eq} of oxygen atoms O2(9e) are modelled using two curves.

Einstein and Debye temperatures (T_{E} and T_{D}) calculated based on $U_{\text{eq}}(T)$ fitting, as well as the difference between the temperatures of the different atoms (Table 5), are comparable to those obtained previously for $(\text{Sm}_{0.93}\text{Bi}_{0.07})\text{Fe}_3(\text{BO}_3)_4$ single crystal [32]. T_{E} and T_{D} of (Sm,Bi) atoms are equal within an error for the single crystal with aluminium content of $y = 0.28$ and for the crystal without Al. T_{E} and T_{D} of (Fe,Al) atoms in the structure of $\text{Sm}_{0.93}\text{Bi}_{0.07}\text{Fe}_{2.72}\text{Al}_{0.28}(\text{BO}_3)_4$ are a little higher (close to an error value) than the T_{E} and T_{D} of Fe atoms in the $(\text{Sm}_{0.93}\text{Bi}_{0.07})\text{Fe}_3(\text{BO}_3)_4$ structure.

Boron atoms had the maximum difference, ΔT_{DE} , corresponding to the largest number of possible vibrational modes, while (Sm,Bi) atoms had the lowest ΔT_{DE} . Boron atoms also had the highest T_{E} and T_{D} , indicating the strongest interaction with neighbouring

atoms. (Sm,Bi) atoms had the lowest T_E and T_D , indicating the weakest interaction with neighbouring atoms.

Temperature dependences of U_{eq} were well fitted using single curves (Table 5, Figure 9a). This agrees with the absence of structural phase transition in the 25–500 K temperature range. However, it was reported earlier that U_{eq} fitting [49] using several curves could be used to detect effects implicit to other structural parameters [58,59]. Therefore, the U_{eq} temperature dependence of boron atoms B2 (9e), having the least smooth character, was fitted over 40–80 K and 110–293 K temperature ranges using two curves. This significantly improved the accuracy of fitting (Figure 9b, Table 5). The chosen low-temperature range of 40–80 K is the identified range of negative thermal expansion (Figure 2). Besides that, including 25 K and 30 K temperature points in the fitting worsened the refinement, which could be due to magnetic phase transition below 40 K. Splitting temperature intervals into two did not improve fitting in the case of B1 (3b) atom, but improved the refinement of O2 (9e) atoms (Figure 9c—modelling curves in the ranges 25–80 K and 110–293 K).

Thus, atomic displacement parameters are sensitive to subtle structural changes in $\text{Sm}_{0.93}\text{Bi}_{0.07}\text{Fe}_{2.72}\text{Al}_{0.28}(\text{BO}_3)_4$, associated with negative thermal expansion.

4. Conclusions

Unit-cell parameters of $\text{Sm}_{1-x}\text{Bi}_x\text{Fe}_{3-y}\text{Al}_y(\text{BO}_3)_4$ ($x = 0.05\text{--}0.07$, $y = 0\text{--}0.28$) single crystals decrease as the aluminium content increases from 0 to 0.28. Temperature dependence of $\text{Sm}_{0.93}\text{Bi}_{0.07}\text{Fe}_{2.72}\text{Al}_{0.28}(\text{BO}_3)_4$ unit-cell parameters do not show any structural phase transition in the 25–500 K temperature range and is similar to that of rare-earth iron borates without $R32 \rightarrow P3_121$ structural phase transition. Negative thermal expansion of $\text{Sm}_{0.93}\text{Bi}_{0.07}\text{Fe}_{2.72}\text{Al}_{0.28}(\text{BO}_3)_4$ was identified below 100 K and was characterized by the characteristic surfaces of the thermal expansion tensor.

No significant anisotropy of electron density close to the (Sm,Bi) and (Fe,Al) positions in $\text{Sm}_{1-x}\text{Bi}_x\text{Fe}_{3-y}\text{Al}_y(\text{BO}_3)_4$ ($x = 0.05\text{--}0.07$, $y = 0\text{--}0.28$) was observed.

(Sm,Bi)–O, (Sm,Bi)–(Fe,Al), (Fe,Al)–(Fe,Al), and (Fe,Al)–O interatomic distances decreased with the addition of aluminium atoms to $\text{Sm}_{1-x}\text{Bi}_x\text{Fe}_{3-y}\text{Al}_y(\text{BO}_3)_4$ ($x = 0.05\text{--}0.07$, $y = 0\text{--}0.28$).

Temperature dependencies of these distances in $\text{Sm}_{0.93}\text{Bi}_{0.07}\text{Fe}_{2.72}\text{Al}_{0.28}(\text{BO}_3)_4$ differed in the region of negative thermal expansion and at higher temperatures. An increase in (Fe,Al)–(Fe,Al) intrachain bond length at low temperatures in the magnetically ordered state could weaken this bond, whereas a decrease in (Fe,Al)–(Fe,Al) interchain distance together with unchanged (Sm,Bi)–(Fe,Al) distance could strengthen super-exchange paths between different chains. Temperature dependence of equivalent isotropic displacement parameters of O2 and B2 atoms vary in the range of negative thermal expansion.

The addition of aluminium atoms influences interatomic distances in $\text{Sm}_{1-x}\text{Bi}_x\text{Fe}_{3-y}\text{Al}_y(\text{BO}_3)_4$ more strongly than lowering the temperature from 293 K to 25 K. Thus, substituting iron atoms in $\text{Sm}_{1-x}\text{Bi}_x\text{Fe}_{3-y}\text{Al}_y(\text{BO}_3)_4$ single crystal with a higher content of Al, as well as substituting iron atoms in $R\text{Fe}_3(\text{BO}_3)_4$ ($R = \text{Eu}\text{--}\text{Er}$) with other metal atoms could influence magnetoelectric properties and structural symmetry.

Supplementary Materials: The following supporting information can be downloaded at <https://www.mdpi.com/article/10.3390/cryst13071128/s1>, Structure information CIF-files: S1–S5 for $\text{Sm}_{1-x}\text{Bi}_x\text{Fe}_{3-y}\text{Al}_y(\text{BO}_3)_4$ ($x = 0.05\text{--}0.07$, $y = 0\text{--}0.28$) at 293 K and CIF S6–S17 for $\text{Sm}_{0.93}\text{Bi}_{0.07}\text{Fe}_{2.72}\text{Al}_{0.28}(\text{BO}_3)_4$ in the temperature range 25–293 K.

Author Contributions: Conceptualization, O.A.A., E.S.S. and K.V.F.; methodology, O.A.A., E.S.S., I.A.G. and K.V.F.; validation, O.A.A., E.S.S. and K.V.F.; formal analysis, E.S.S., O.A.A. and K.V.F.; crystal growth, I.A.G.; EDX analysis, V.V.A. and D.N.K.; XRF analysis, T.A.S. and E.S.S.; single-crystal XRD, E.S.S. and E.V.S.; data curation, E.S.S., V.V.A., E.V.S., T.A.S., D.N.K. and I.A.G.; writing—original draft preparation, E.S.S., I.A.G., O.A.A. and K.V.F.; writing—review and editing, O.A.A., K.V.F. and E.S.S.; visualization, E.S.S.; supervision, O.A.A. and K.V.F.; project administration, O.A.A. and K.V.F. All authors have read and agreed to the published version of the manuscript.

Funding: This work was supported by the Russian Science Foundation (project No 23-22-00286).

Data Availability Statement: Crystal structure datasets were deposited via the joint CCDC/FIZ Karlsruhe deposition service at <https://www.ccdc.cam.ac.uk> (accessed on 14 July 2023) and assigned Deposition Numbers CSD 2271124–2271140.

Acknowledgments: This work was conducted using equipment at the Shared Research Center FSRC ‘Crystallography and Photonics’ RAS.

Conflicts of Interest: The authors declare no conflict of interest.

Appendix A

The appendix presents a comparison of reflection indexation in monoclinic and trigonal unit cells of $\text{Sm}_{0.93}\text{Bi}_{0.07}\text{Fe}_{2.72}\text{Al}_{0.28}(\text{BO}_3)_4$ single crystals at 25 K. 3D diffraction patterns were collected using XtaLAB Synergy-DW diffractometer with HyPix-Arc 150° detector and rotating anode (Mo $K\alpha$ radiation). UB-matrix fitting of the monoclinic unit cell with parameters $a = 7.4737(3) \text{ \AA}$, $b = 9.5516(3) \text{ \AA}$, $c = 11.4930(5) \text{ \AA}$, $\beta = 103.820(4)$ was performed using 18 145 observed reflections out of 18 177 total reflections (99.82%). UB fitting of the trigonal unit cell was performed using 18 165 observed reflections out of 18 177 total reflections (99.93%). However, visual analysis of the monoclinic lattice chosen highlights the wrong choice of unit cell since reflections in the reciprocal lattice points were regularly absent in the case of the monoclinic unit cell (Figure A1a), whereas all reciprocal lattice points contained reflections in the case of the trigonal lattice (Figure A1b). Although reflections in the monoclinic space group $C2/c$ were averaged with $R_{\text{int}} = 9.01\%$ (which is comparable to averaging in trigonal space group $R32$, Table 3), the search for the initial model of heavy atoms was not successful in the $C2/c$ space group and the refinement of the initial structure model from [21] failed when refinement factor $R > 20\%$.

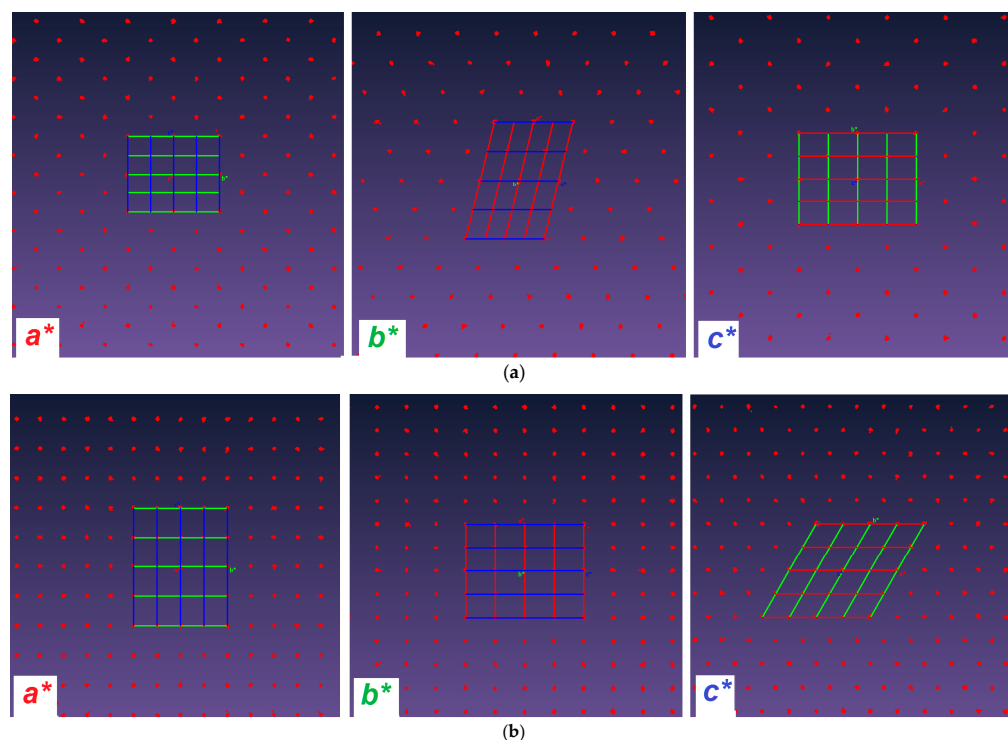


Figure A1. View of the three-dimensional diffraction peak distribution in the [100], [010], and [001] directions of $\text{Sm}_{0.93}\text{Bi}_{0.07}\text{Fe}_{2.72}\text{Al}_{0.28}(\text{BO}_3)_4$ at 25 K: (a) monoclinic lattice and (b) trigonal lattice. None reflections were rejected to show in the figure. Reciprocal lattice lines in the directions of a^* , b^* , c^* are shown by different colours.

References

1. Kuz'micheva, G.; Kaurova, I.; Rybakov, V.; Podbel'skiy, V. Crystallochemical Design of Huntite-Family Compounds. *Crystals* **2019**, *9*, 100. [[CrossRef](#)]
2. Kadomtseva, A.M.; Popov, Y.F.; Vorob'ev, G.P.; Pyatakov, A.P.; Krotov, S.S.; Kamilov, K.I.; Ivanov, V.Y.; Mukhin, A.A.; Zvezdin, A.K.; Kuz'menko, A.M.; et al. Magnetolectric and Magnetoelastic Properties of Rare-Earth Ferrobates. *Low Temp. Phys.* **2010**, *36*, 511–521. [[CrossRef](#)]
3. Vasiliev, A.N.; Popova, E.A. Rare-Earth Ferrobates $RFe_3(BO_3)_4$. *Low Temp. Phys.* **2006**, *32*, 735–747. [[CrossRef](#)]
4. Kuz'menko, A.M.; Mukhin, A.A.; Ivanov, V.Y.; Kadomtseva, A.M.; Bezmaternykh, L.N. Effects of the Interaction between R and Fe Modes of the Magnetic Resonance in $RFe_3(BO_3)_4$ Rare-Earth Iron Borates. *JETP Lett.* **2011**, *94*, 294–300. [[CrossRef](#)]
5. Kuzmenko, A.M.; Szaller, D.; Kain, T.; Dziom, V.; Weymann, L.; Shuvaev, A.; Pimenov, A.; Mukhin, A.A.; Ivanov, V.Y.; Gudim, I.A.; et al. Switching of Magnons by Electric and Magnetic Fields in Multiferroic Borates. *Phys. Rev. Lett.* **2018**, *120*, 027203. [[CrossRef](#)]
6. Popova, M.N.; Boldyrev, K.N.; Klimin, S.A.; Stanislavchuk, T.N.; Sirenko, A.A.; Bezmaternykh, L.N. Spectral Signatures of Spin-Phonon and Electron-Phonon Interactions in Multiferroic Iron Borates. *J. Magn. Magn. Mater.* **2015**, *383*, 250–254. [[CrossRef](#)]
7. Hinatsu, Y.; Doi, Y.; Ito, K.; Wakeshima, M.; Alemi, A. Magnetic and Calorimetric Studies on Rare-Earth Iron Borates $LnFe_3(BO_3)_4$ ($Ln = Y, La-Nd, Sm-Ho$). *J. Solid. State Chem.* **2003**, *172*, 438–445. [[CrossRef](#)]
8. Ritter, C.; Pankrats, A.; Gudim, I.; Vorotynov, A. Determination of the Magnetic Structure of $SmFe_3(BO_3)_4$ by Neutron Diffraction: Comparison with Other $RFe_3(BO_3)_4$ Iron Borates. *J. Phys. Condens. Matter.* **2012**, *24*, 386002. [[CrossRef](#)]
9. Popov, Y.F.; Kadomtseva, A.M.; Vorob'ev, G.P.; Mukhin, A.A.; Ivanov, V.Y.; Kuz'menko, A.M.; Prokhorov, A.S.; Bezmaternykh, L.N.; Temerov, V.L. Observation of Spontaneous Spin Reorientation in $Nd_{1-x}Dy_xFe_3(BO_3)_4$ Ferrobates with a Competitive R-Fe Exchange. *JETP Lett.* **2009**, *89*, 345–351. [[CrossRef](#)]
10. Liang, K.-C.; Chaudhury, R.P.; Lorenz, B.; Sun, Y.Y.; Bezmaternykh, L.N.; Temerov, V.L.; Chu, C.W. Giant Magnetolectric Effect in $HoAl_3(BO_3)_4$. *Phys. Rev. B* **2011**, *83*, 180417. [[CrossRef](#)]
11. Liang, K.-C.; Chaudhury, R.P.; Lorenz, B.; Sun, Y.Y.; Bezmaternykh, L.N.; Gudim, I.A.; Temerov, V.L.; Chu, C.W. Magnetolectricity in the System $RA_3(BO_3)_4$ ($R = Tb, Ho, Er, Tm$). *J. Phys. Conf. Ser.* **2012**, *400*, 032046. [[CrossRef](#)]
12. Sváb, E.; Beregi, E.; Fábrián, M.; Mészáros, G. Neutron Diffraction Structure Study of Er and Yb Doped $YAl_3(BO_3)_4$. *Opt. Mater.* **2012**, *34*, 1473–1476. [[CrossRef](#)]
13. Kadomtseva, A.M.; Kuvardin, A.V.; Pyatakov, A.P.; Zvezdin, A.K.; Vorob'ev, G.P.; Popov, Y.F.; Bezmaternykh, L.N. Magnetic Magnetolectric and Magnetoelastic Properties of New Multiferroic Material $NdFe_3(BO_3)_4$. *arXiv* **2006**, arXiv:cond-mat/0607217v1. [[CrossRef](#)]
14. Klimin, S.A.; Fausti, D.; Meetsma, A.; Bezmaternykh, L.N.; Van Loosdrecht, P.H.M.; Palstra, T.T.M. Evidence for Differentiation in the Iron-Helicoidal Chain in $GdFe_3(BO_3)_4$. *Acta Crystallogr. B* **2005**, *61*, 481–485. [[CrossRef](#)] [[PubMed](#)]
15. Alekseeva, O.A.; Smirnova, E.S.; Frolov, K.V.; Lyubutina, M.V.; Lyubutin, I.S.; Gudim, I.A. Crystal Structure Dynamics of $RFe_3(BO_3)_4$ Single Crystals in the Temperature Range 25–500 K. *Crystals* **2022**, *12*, 1203. [[CrossRef](#)]
16. Zvezdin, A.K.; Krotov, S.S.; Kadomtseva, A.M.; Vorob'ev, G.P.; Popov, Y.F.; Pyatakov, A.P.; Bezmaternykh, L.N.; Popova, E.A. Magnetolectric Effects in Gadolinium Iron Borate $GdFe_3(BO_3)_4$. *J. Exp. Theor. Phys. Lett.* **2005**, *81*, 272–276. [[CrossRef](#)]
17. Frolov, K.V.; Lyubutin, I.S.; Smirnova, E.S.; Alekseeva, O.A.; Verin, I.A.; Artemov, V.V.; Kharlamova, S.A.; Bezmaternykh, L.N.; Gudim, I.A. Low-Temperature Structural and Magnetic Phase Transitions in Multiferroic $GdFe_3(BO_3)_4$. *J. Alloys Compd.* **2016**, *671*, 545–551. [[CrossRef](#)]
18. Ritter, C.; Balaev, A.; Vorotynov, A.; Petrakovskii, G.; Velikanov, D.; Temerov, V.; Gudim, I. Magnetic Structure, Magnetic Interactions and Metamagnetism in Terbium Iron Borate $TbFe_3(BO_3)_4$: A Neutron Diffraction and Magnetization Study. *J. Phys. Condens. Matter* **2007**, *19*, 196227. [[CrossRef](#)]
19. Ritter, C.; Vorotynov, A.; Pankrats, A.; Petrakovskii, G.; Temerov, V.; Gudim, I.; Szymczak, R. Magnetic Structure in Iron Borates $RFe_3(BO_3)_4$ ($R = Y, Ho$): A Neutron Diffraction and Magnetization Study. *J. Phys. Condens. Matter* **2008**, *20*, 365209. [[CrossRef](#)]
20. Kadomtseva, A.M.; Vorob'ev, G.P.; Popov, Y.F.; Pyatakov, A.P.; Mukhin, A.A.; Ivanov, V.Y.; Zvezdin, A.K.; Gudim, I.A.; Temerov, V.L.; Bezmaternykh, L.N. Magnetolectric and Magnetoelastic Properties of Easy-Plane Ferrobates with a Small Ionic Radius. *J. Exp. Theor. Phys.* **2012**, *114*, 810–817. [[CrossRef](#)]
21. Oreshonkov, A.S.; Shestakov, N.P.; Molokeev, M.S.; Aleksandrovsky, A.S.; Gudim, I.A.; Temerov, V.L.; Adichtchev, S.V.; Pugachev, A.M.; Nemtsev, I.V.; Pogoreltsev, E.I.; et al. Monoclinic $SmAl_3(BO_3)_4$: Synthesis, Structural and Spectroscopic Properties. *Acta Crystallogr. B Struct. Sci. Cryst. Eng. Mater.* **2020**, *76*, 654–660. [[CrossRef](#)] [[PubMed](#)]
22. Dobretsova, E.A.; Borovikova, E.Y.; Boldyrev, K.N.; Kurazhkovskaya, V.S.; Leonyuk, N.I. IR Spectroscopy of Rare-Earth Aluminum Borates $RA_3(BO_3)_4$ ($R = Y, Pr-Yb$). *Opt. Spectrosc.* **2014**, *116*, 77–83. [[CrossRef](#)]
23. Plachinda, P.A.; Belokoneva, E.L. High Temperature Synthesis and Crystal Structure of New Representatives of the Huntite Family. *Cryst. Res. Technol.* **2008**, *43*, 157–165. [[CrossRef](#)]
24. Dobretsova, E.A.; Boldyrev, K.N.; Popova, M.N.; Chernyshev, V.A.; Borovikova, E.Y.; Maltsev, V.V.; Leonyuk, N.I. Vibrational Spectroscopy of $GdCr_3(BO_3)_4$: Quantitative Separation of Crystalline Phases. *J. Phys. Conf. Ser.* **2016**, *737*, 012035. [[CrossRef](#)]
25. Leonyuk, N.I.; Maltsev, V.V.; Volkova, E.A.; Koporulina, E.V.; Kuleshov, N.V.; Kisel, V.E.; Gorbachenya, K.N. Ytterbium and Erbium Co-Doped Rare-Earth Aluminum Borate Crystals as New Materials for Eye-Safe Lasers: Flux Growth and Characterization. In *Handbook of Ecomaterials*; Springer International Publishing: Cham, Switzerland, 2019; pp. 2491–2536.

26. Leonyuk, N.I.; Leonyuk, L.I. Growth and Characterization of $RM_3(BO_3)_4$ Crystals. *Prog. Cryst. Growth Charact. Mater.* **1995**, *31*, 179–278. [CrossRef]
27. Boldyrev, K.N.; Popova, M.N.; Bettinelli, M.; Temerov, V.L.; Gudim, I.A.; Bezmaternykh, L.N.; Loiseau, P.; Aka, G.; Leonyuk, N.I. Quality of the Rare Earth Aluminum Borate Crystals for Laser Applications, Probed by High-Resolution Spectroscopy of the Yb^{3+} Ion. *Opt. Mater.* **2012**, *34*, 1885–1889. [CrossRef]
28. Gudim, I.A.; Eremin, E.V.; Temerov, V.L. Flux Growth and Spin Reorientation in Trigonal $Nd_{1-x}Dy_xFe_3(BO_3)_4$ Single Crystals. *J. Cryst. Growth* **2010**, *312*, 2427–2430. [CrossRef]
29. Eremin, E.; Gudim, I.; Temerov, V.; Smolyakov, D.; Molokeyev, M. Comparing the Magnetic and Magnetoelectric Properties of the $SmFe_3(BO_3)_4$ Ferroborate Single Crystals Grown Using Different Solvents. *J. Cryst. Growth* **2019**, *518*, 1–4. [CrossRef]
30. Bezmaternykh, L.N.; Temerov, V.L.; Gudim, I.A.; Stolbovaya, N.A. Crystallization of Trigonal $(Tb,Er)(Fe,Ga)_3(BO_3)_4$ Phases with Hantite Structure in Bismuth Trimolybdate-Based Fluxes. *Crystallogr. Rep.* **2005**, *50*, S97–S99. [CrossRef]
31. Bezmaternykh, L.N.; Kharlamova, S.A.; Temerov, V.L. Flux Crystallization of Trigonal $GdFe_3(BO_3)_4$ Competing with the Crystallization of $\alpha-Fe_2O_3$. *Crystallogr. Rep.* **2004**, *49*, 855–857. [CrossRef]
32. Smirnova, E.S.; Alekseeva, O.A.; Dudka, A.P.; Sorokin, T.A.; Khmelenin, D.N.; Yapaskurt, V.O.; Lyubutina, M.V.; Frolov, K.V.; Lyubutin, I.S.; Gudim, I.A. Crystal Structure, Absolute Configuration and Characteristic Temperatures of $SmFe_3(BO_3)_4$ in the Temperature Range 11–400 K. *Acta Crystallogr. B Struct. Sci. Cryst. Eng. Mater.* **2022**, *78*, 546–556. [CrossRef] [PubMed]
33. Maltsev, V.V.; Volkova, E.A.; Mitina, D.D.; Leonyuk, N.I.; Kozlov, A.B.; Shestakov, A.V. Growth and Thermophysical Properties of $RA_3(BO_3)_4$ ($R = Y, Nd, Gd, Lu$) and $RMgB_5O_{10}$ ($R = Y, La, Gd$) Crystals. *Inorg. Mater.* **2020**, *56*, 612–625. [CrossRef]
34. Leonyuk, N.I.; Maltsev, V.V.; Volkova, E.A.; Pilipenko, O.V.; Koporulina, E.V.; Kisel, V.E.; Tolstik, N.A.; Kurilchik, S.V.; Kuleshov, N.V. Crystal Growth and Laser Properties of New $RA_3(BO_3)_4$ ($R = Yb, Er$) Crystals. *Opt. Mater.* **2007**, *30*, 161–163. [CrossRef]
35. Mukhin, A.A.; Vorob'ev, G.P.; Ivanov, V.Y.; Kadomtseva, A.M.; Narizhnaya, A.S.; Kuz'menko, A.M.; Popov, Y.F.; Bezmaternykh, L.N.; Gudim, I.A. Colossal Magnetodielectric Effect in $SmFe_3(BO_3)_4$ Multiferroic. *JETP Lett.* **2011**, *93*, 275–281. [CrossRef]
36. Trukhanov, A.V.; Kostishyn, V.G.; Panina, L.V.; Korovushkin, V.V.; Turchenko, V.A.; Thakur, P.; Thakur, A.; Yang, Y.; Vinnik, D.A.; Yakovenko, E.S.; et al. Control of Electromagnetic Properties in Substituted M-Type Hexagonal Ferrites. *J. Alloys Compd.* **2018**, *754*, 247–256. [CrossRef]
37. Snegirev, N.I.; Bogach, A.V.; Lyubutin, I.S.; Chuev, M.A.; Yagupov, S.V.; Mogilenec, Y.A.; Selezneva, K.A.; Strugatsky, M.B. The Evolution of the Magnetic Properties of Iron Borate Single Crystals Doped with Gallium. *Phys. Met. Metallogr.* **2023**, *124*, 133–137. [CrossRef]
38. Kumar, A.; Sharma, P.; Kumar, S.; Singh, A.; Kundu, R.S.; Punia, R. Effect of Diamagnetic Ion Substitution on Structural and Magnetic Properties of Nd^{3+} Modified Solid Solutions. *Integr. Ferroelectr.* **2019**, *203*, 176–182. [CrossRef]
39. Jahan, N.; Khandaker, J.I.; Liba, S.I.; Hoque, S.M.; Khan, M.N.I. Structural Analysis through Cations Distributions of Diamagnetic Al^{3+} Ions Substituted Ni-Zn-Co Ferrites. *J. Alloys Compd.* **2021**, *869*, 159226. [CrossRef]
40. Smirnova, E.S.; Alekseeva, O.A.; Dudka, A.P.; Verin, I.A.; Artemov, V.V.; Lyubutina, M.V.; Gudim, I.A.; Frolov, K.V.; Lyubutin, I.S. Crystal Structure of Bismuth-Containing $NdFe_3(BO_3)_4$ in the Temperature Range 20–500 K. *Acta Crystallogr. B Struct. Sci. Cryst. Eng. Mater.* **2022**, *78*, 1–13. [CrossRef]
41. CrysAlisPro Software System; Rigaku Corporation: Wroclaw, Poland. Available online: <http://www.rigaku.com> (accessed on 14 July 2023).
42. Petříček, V.; Dušek, M.; Palatinus, L. Crystallographic Computing System JANA2006: General Features. *Z. Krist. Cryst. Mater.* **2014**, *229*, 345–352. [CrossRef]
43. Shannon, R.D. *Revised Effective Ionic Radii and Systematic Studies of Interatomic Distances in Halides and Chalcogenides*; Wiley Online Library: Hoboken, NJ, USA, 1976; Volume 32.
44. Atomistic Simulation Group in the Materials Department of Imperial College Database of Ionic Radii. Available online: <http://abulafia.mt.ic.ac.uk/shannon/ptable.php> (accessed on 21 June 2023).
45. Watkin, D.J.; Cooper, R.I. Howard Flack and the Flack Parameter. *Chemistry* **2020**, *2*, 796–804. [CrossRef]
46. Becker, P.J.; Coppens, P. Extinction within the Limit of Validity of the Darwin Transfer Equations. I. General Formalism for Primary and Secondary Extinction and Their Applications to Spherical Crystals. *Acta Crystallogr. Sect. A* **1974**, *30*, 129–147. [CrossRef]
47. Becker, P.J.; Coppens, P. Extinction within the Limit of Validity of the Darwin Transfer Equations. II. Refinement of Extinction in Spherical Crystals of SrF_2 and LiF . *Acta Crystallogr. Sect. A* **1974**, *30*, 148–153. [CrossRef]
48. Bubnova, R.S.; Firsova, V.A.; Filatov, S.K. Software for Determining the Thermal Expansion Tensor and the Graphic Representation of Its Characteristic Surface (Theta to Tensor-TTT). *Glass Phys. Chem.* **2013**, *39*, 347–350. [CrossRef]
49. Dudka, A.P.; Bolotina, N.B.; Khrykina, O.N. DebyeFit: A Simple Tool to Obtain an Appropriate Model of Atomic Vibrations in Solids from Atomic Displacement Parameters Obtained at Different Temperatures. *J. Appl. Crystallogr.* **2019**, *52*, 690–692. [CrossRef]
50. Momma, K.; Ikeda, T.; Belik, A.A.; Izumi, F. Dysnomia, a Computer Program for Maximum-Entropy Method (MEM) Analysis and Its Performance in the MEM-Based Pattern Fitting. *Powder Diffr.* **2013**, *28*, 184–193. [CrossRef]
51. Stoiber, D.; Niewa, R.; Kristallogr, Z. Available online: <https://www.iac.uni-stuttgart.de/en/research/akniewa/downloads/> (accessed on 14 July 2023).

52. Campá, J.A.; Cascales, C.; Gutiérrez-Puebla, E.; Monge, M.A.; Rasines, I.; Ruíz-Valero, C. Crystal Structure, Magnetic Order, and Vibrational Behavior in Iron Rare-Earth Borates. *Chem. Mater.* **1997**, *9*, 237–240. [[CrossRef](#)]
53. Massa, W.; Gould, R.O. *Crystal Structure Determination*; SpringerLink: Berlin/Heidelberg, Germany, 2004.
54. Poray-Koshits, M.A. *Fundamentals of Structural Analysis of Chemical Compounds*; HSE Publishing House: Moscow, Russia, 1982. (In Russian)
55. Belokoneva, E.L.; Al'shinskaya, L.I.; Simonov, M.A.; Leonyuk, N.I.; Timchenko, T.I.; Belov, N.V. Crystal Structure of NdGa₃[BO₃]₄. *J. Struct. Chem.* **1978**, *19*, 332–334. [[CrossRef](#)]
56. Eremin, E.V.; Pavlovskiy, M.S.; Gudim, I.A.; Temerov, V.; Molokeyev, M.; Andryushin, N.D.; Bogdanov, E.V. Synthesis of NdSc₃(BO₃)₄ Single Crystals and Study of Its Structure Properties. *J. Alloys Compd.* **2020**, *828*, 154355. [[CrossRef](#)]
57. Chong, S.; Riley, B.J.; Nelson, Z.J.; Perry, S.N. Crystal Structures and Comparisons of Huntite Aluminum Borates RE Al₃(BO₃)₄ (RE = Tb, Dy and Ho). *Acta Crystallogr. E Crystallogr. Commun.* **2020**, *76*, 339–343. [[CrossRef](#)]
58. Bolotina, N.; Khrykina, O.; Azarevich, A.; Gavrilkin, S.; Sluchanko, N. Fine Details of Crystal Structure and Atomic Vibrations in YbB₁₂ with a Metal–Insulator Transition. *Acta Crystallogr. B Struct. Sci. Cryst. Eng. Mater.* **2020**, *76*, 1117–1127. [[CrossRef](#)] [[PubMed](#)]
59. Inosov, D.S. *Rare-Earth Borides*; Jenny Stanford Publishing: New York, NY, USA, 2021; ISBN 9781003146483.

Disclaimer/Publisher's Note: The statements, opinions and data contained in all publications are solely those of the individual author(s) and contributor(s) and not of MDPI and/or the editor(s). MDPI and/or the editor(s) disclaim responsibility for any injury to people or property resulting from any ideas, methods, instructions or products referred to in the content.